國立交通大學

光電工程學系碩士班

碩 士 論 文

銅銦鎵硒薄膜太陽能電池中化學水浴法製備之硫化鋅緩衝層製程技術優化

The Zinc Sulfide Buffer Layer Fabrication Using Chemical Bath Deposition Processes in $Cu(In,Ga)Se_2$ Thin Film Solar cells

研 究 生：白　諭

指導教授：謝漢萍 教授

黃乙白 副教授

中 華 民 國 一百零一 年 十一 月

銅銦鎵硒薄膜太陽能電池中化學水浴法製備之硫化鋅緩衝層製程技術優化

The Zinc Sulfide buffer layer fabrication using chemical bath deposition processes in $Cu(In,Ga)Se_2$ thin film solar cells

研 究 生：白　諭　　Student：Che-Hsuan Yang

指導教授：謝漢萍　　Advisor：Han-Ping D. Shieh

黃乙白　　Yi-Pai Huang

國 立 交 通 大 學

光 電 工 程 學 系 碩 士 班

碩 士 論 文

A Thesis
Submitted to Department of Electro-Optical Engineering
College of Electrical and Computer Engineering
National Chiao Tung University
in partial Fulfillment of the Requirements
for the Degree of
Master
in
Electro-Optical Engineering
July 2012
Hsinchu, Taiwan, Republic of China

中華民國一百零一年十一月

銅銦鎵硒薄膜太陽能電池中化學水浴法製備之硫化鋅緩衝層製程技術優化

學生：白諭　　指導教授：謝漢萍教授
黃乙白副教授

國立交通大學電機學院　　光電工程學系碩士班

摘 要

銅銦鎵硒是一種具有潛力的薄漠太陽能電池材料，目前其最高轉換效率達到20.3%。然而在高效率太陽能電池的生產過程中，其緩衝層材料所使用的硫化鎘由於包含了鎘的成分，在電池年限到達之後將會對環境造成汙染。因此本論文提出對環境影響較小，同時不會嚴重降低電池效率的緩衝材料硫化鋅。由於硫化鋅本身是活性較低的材料，不容易在銅銦鎵硒吸收層上形成高覆蓋率與適當鋅硫化學當量比的薄膜，因此本論文針對化學水浴法製備之硫化鋅緩衝層做研究，包含了薄膜覆蓋率、鋅與硫化學當量比、薄膜厚度三者的改善。論文中首先研究了溶液中的溫度、氨水濃度、沉積時間對薄膜品質的影響，經由分析硫化鋅在化學水浴法中的沉膜機制後，提出了兩種增進成膜品質的方法，分別為「後處理製程」與「兩階段製程」。進一步研究「後處理製程」與「兩階段製程」發現兩階段製程可以有效增進硫化鋅的成膜品質，硫化鋅的兩階段製程在銅銦鎵硒吸收層上只需沉積大約 100 奈米的薄膜厚度即可達到了超過 95 %的薄膜覆蓋率、1.78 鋅與硫化學當量比。

The Zinc Sulfide buffer layer fabrication using chemical bath deposition processes in Cu(In,Ga)Se_2 thin film solar cells

Student: Ian Pai

Advisor: Prof. Han-Ping D. Shieh
Prof. Yi-Pai Huang

Dept. of Photonics & Institute of Electro-Optical Engineering
National Chiao Tung University

Abstract

Thin film Copper Indium Gallium Diselenide CIGS (CIGS) solar cells are one of the most promising candidates. Until now, the latest world record CIGS solar cell has achieved 20.3 % in efficiency. However, in CIGS solar cells fabrication, the use of cadmium sulfide as buffer layer in CIGS solar cells contaminates the environments when the solar cell panels reach lifetime. Therefore, the buffer material zinc sulfide (ZnS) which rarely affects the environments and does not decrease the cell efficiency largely was studied in this thesis. ZnS is a low activation material, so it is difficult to deposit high coverage and suitable stoichiometric ratio ZnS thin-film on CIGS absorber layer. Therefore, the aim of this study is to develop a deposition method for

the ZnS buffer layer to reach desired Zn/S stoichiometric ratio and to improve coverage properties by using chemical bath deposition (CBD). Firstly, the temperature, the ammonia concentration, and the deposition time in chemical bath solution were investigated on the film properties. By analyzing the ZnS film growth mechanism in CBD method, two deposition methods, post-deposition and two-step deposition, are proposed. Through further investigation of the post-deposition and the two-step deposition, the two-step deposition method improves the ZnS film properties effectively. The ZnS film deposited by two-step deposition only needs to deposit about 100 nm thickness and then can reach over 95 % coverage properties and 1.78 Zn/S stoichiometric ratios on CIGS absorber layer.

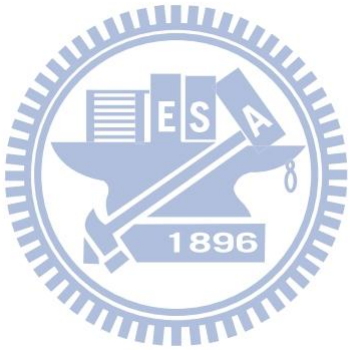

誌 謝

首先最誠摯感謝實驗室的兩位大家長：謝漢萍老師與黃乙白老師，兩位老師在研究、態度、和報告上的指導與培養，使我在碩士生涯中能夠學習到不少的研究知識、上台報告的技巧與做事情的態度，此外要感謝兩位老師提供豐富的資源與完善的研究環境，讓此論文得以順利完成。另外，更要感謝每位口試委員所提供的寶貴意見，使得本論文更加完善。

此篇論文能夠順利完成要特別感謝蔡柏全學長、王奕智學長與蔡韻竹學姊的指導。兩年來，三位學長姐一路引導、協助並且鼓勵我，讓我在學術上或是生活上學習到很多觀念與方法，讓我在碩士階段成長了不少。也要感謝同組的學長姐們，濟宇以及子寬，在這兩年來的指導與協助，當我有問題時不吝惜的給我幫助及建議。

兩年的研究生活，感謝大頭哥哥，致維哥、芳正、志明、台翔、精益、國振等學長姐們提供各方面的指導與分享，也謝謝小馬、思頤、小頭、小董、馬爺、博六、博詮、立偉、小 fighter，讓我的生活更加精彩。感謝拉拉、博凱、囧務陪我度過了很多難熬的時刻，另外還有博鈞、上翰、秉彥、柏皓、岡儒陪我一起留下了美好且精彩的回憶。和你們在課業、研究與生活上的討論與分享讓我又有了不同的想法與開心的心情。也感謝米克、阿昌、小岡、小靖、登曜、小黑與雍仁等學弟們在諸多事情上的幫助。再來還要謝謝助理姐姐們，雅惠、穎佳、茉莉、蓮芳在各方面事情的處理上盡了很多心力，讓我們毫無後顧之憂也讓實驗室充滿了歡樂的氣氛。

最重要的，我要感謝我最親愛的家人，謝謝爸媽的支持與鼓勵和妹妹的關心，讓我在求學路程上可以毫無顧慮的專注在學習的部分。最後，我要將這份喜悅分享給一路走來支持我的各位。

Table of Contents

Figure Captions

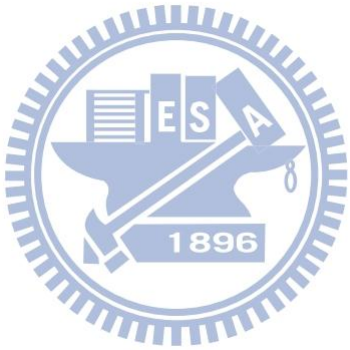

Table Captions

Chapter 1 Introduction

Energy resources like oil, gas, and coal are mainly used in recent decades, but the cost has gradually become high due to the limited energy resources on Earth. In addition, when these fossil fuels are consumed, carbon dioxide from the production process causes the Earth's greenhouse, melting glaciers, and climate anomalies. Therefore, for natural environments, clean, renewable, and sustainable energy is indispensable.

1.1 Solar Energy Background

As the development of science and technology continues, the consumption of energy significantly increases. The reverses of the energy resources such as oil, gas, and coal are limited on Earth and will be depleted one day in the future, so the development of renewable energy has risen progressively. The prediction of energy usage in the world is demonstrated in Fig. 1. So far in 2012, oil, gas, and coal are the major supply for the energy used. Accompanying with the reduction of oil, gas, and coal, renewable energy such as biomass, wind, and solar energy has become more important. Among these renewable energy resources, solar energy is believed to become a major power generation in the future because of its unlimited, pollution-free, and wide-spread characteristics. However, solar energy has some issues such as instability under different weather condition and high installation cost. Thus, many research institutions and industries have been working on improving the conversion efficiency, reducing costs, and developing mass production of solar cells.

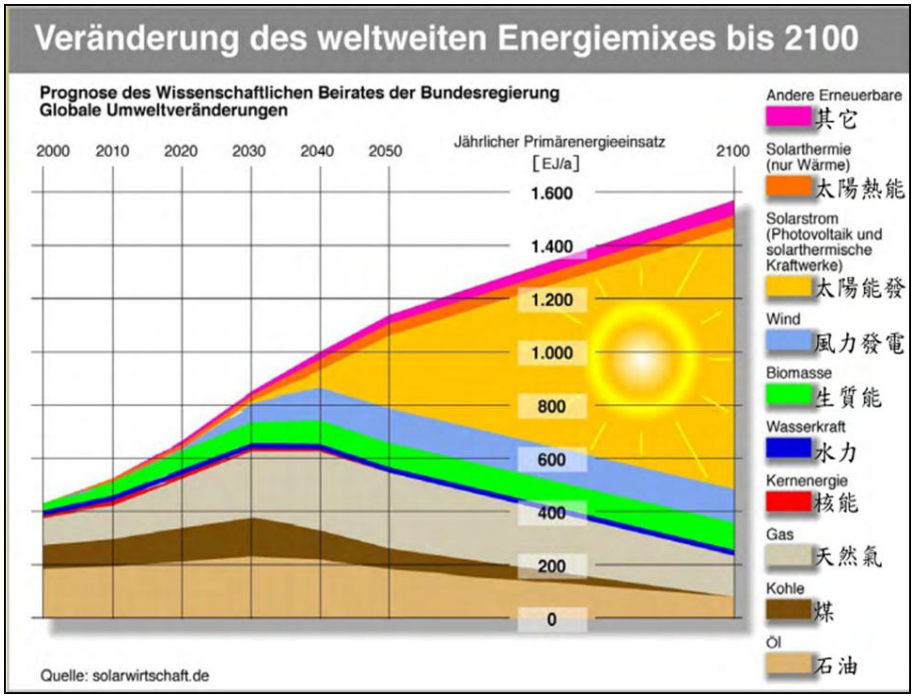

Fig. 1 The prediction of energy usage in the world

So far, the classification of solar cells can be divided into three categories: (1) the first generation: wafer-based solar cells, (2) the second generation: thin film solar cells, and (3) the third generation: organic and nanotechnology solar cells. The following is detailed description of each generation.

Silicon wafers were widely used in the semiconductor industry. Building on the experience of the semiconductor industry, the manufacturing technologies of wafer-based solar cells were already quite mature. Wafer-based solar cells included single-crystalline and multi-crystalline solar cells. Single-crystalline solar cells which had high cost and complex fabrication process achieved around 25% [1] in efficiency. In contrast, multi-crystalline solar cells were proposed and reached about 20% [2] in efficiency because of the lower cost and simplified fabrication process compared with single-crystalline solar cells. Nevertheless, some issues from wafer-based solar cells had to be concerned, including high cost, indirect band-gap, and low absorption coefficient properties.

Unlike the first-generation solar cells, the second generation solar cells were developed to improve the cell efficiency by selecting different materials. The materials like copper indium diselenide (CIS or $CuInSe_2$), cadmium telluride (CdTe), and hydrogenated amorphous silicon (a-Si:H) were selected (as shown in Fig. 2) because of their high optical absorption coefficient and thin material usage which was enough to absorb most sunlight effectively. Generally, the second generation solar cells were also called thin film solar cells. Moreover, in thin film solar cells, the reduced usage of materials was adapted to combine with inexpensive substrates such as glass, flexible plastic, and stainless steel for decreasing the cost.

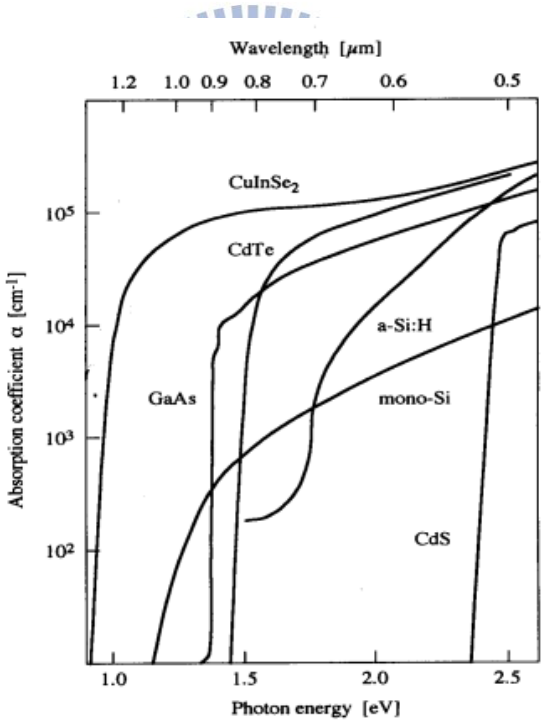

Fig. 2 Absorption coefficients of various semiconductor materials

The third generation solar cells could be divided into two types: macromolecule solar cells and organic solar cells. Both types had the advantages such as low cost, simple production, and wide application. In addition, the portable and foldable

characteristics in macromolecule and organic solar cells could be used in cell phones, clothing, backpacks, tents, and many daily necessities.

Among three generations, the second generation solar cells is preferred because of its low cost compared to the first generation solar cells and its mature technology compared to the third generation solar cells. In the second generation solar cells, CIS, CdTe, and a-Si:H are the high optical absorption compounds. Many researchers have dedicated to optimize the fabrication of the aforementioned compounds for achieving high conversion efficiency. CIS material shows relatively high absorptivity among these materials as shown in Fig. 2. Almost the entire incident light is absorbed within the first micrometer of the CIS film. Furthermore, the band-gap of CIS compound can be dominated between 1.0 and 1.7 eV by doping small amounts of Gallium (Ga) into the CIS film to form copper indium gallium diselenide (CIGS), which further increases the absorption of sunlight.

For the cell efficiency in laboratory and module efficiency in corporation of the present investigation, CIGS solar cells are 20.3% (0.503 cm^2) and 15.7% (9703 cm^2), CdTe solar cells are 16.7% (1.032 cm^2) and 12.8% (6687 cm^2),as well as a-Si:H solar cells are 12.5% (0.27 cm^2) and 10.4% (905 cm^2) [3], respectively. The results demonstrate the efficiency of CIGS is the best of three thin film materials. Besides the efficiencies of solar cells, a material which is harmful to the environment should be discussed. For CdTe, Cadmium (Cd) causes environmental pollution during the manufactory as well as the problem of how to deal with contaminants when the solar cell panels reach lifetime.

To summarize the above factors, CIS or CIGS has the potential to be the new candidate in solar cells materials for its low production cost, high conversion efficiency, and toxic-free capability.

1.2 CIGS Thin Film Solar Cells

The first CIS photovoltaic device appeared in 1973 when a research team at Salford University annealed $CuInSe_2$ in indium [4]. So far, CIGS solar cells have reached 20.3% in efficiency [5] at the size of laboratory-scale by Zentrum fuer Sonnenenergie und Wasserstoff-Forschung (ZSW), in Baden-Wuerttemberg, Germany. The cells setup of each layer can be described as following: soda-lime glass (SLG) as a substrate, sputtered molybdenum (Mo) as back contact metal, co-evaporated CIGS as absorber layer, chemical bath deposited cadmium sulfide (CdS) as buffer layer, sputtered intrinsic zinc oxide (i-ZnO) and sputtered aluminum-doped ZnO (ZnO:Al) as window layer, sputtered surface-structural MgF_2 as anti-reflection layer, and a nickel (Ni)/aluminum (Al)-grid as front contact. A schematic of CIGS thin film solar cells from ZSW is demonstrated in Fig. 3.

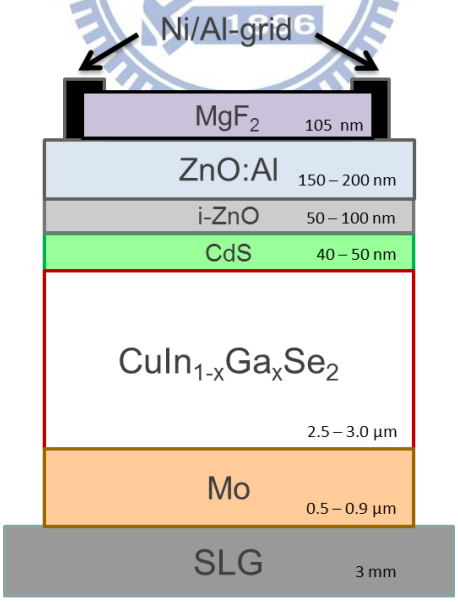

Fig. 3 The structure of latest world record CIGS solar cells [5]

Prof. Ingvid Repius, National Renewable Energy Lab (NREL), USA, provided the similar cell fabrication, and the cell efficiency achieved 19.9% [6]. Prof. Tokio

Nakada from Aoyama Gakuin University (AGU), Japan, proposed the CIGS solar cell with the toxic-free buffer material zinc sulfide (ZnS), and the cell efficiency achieved 18.6% [7]. The simple comparisons of CIGS solar cells fabricated by these three research institutions are listed in Table 1.

Table 1 Comparisons of CIGS solar cells in cell fabrication

Institutes	CIGS deposition	Buffer material	Window layer	Efficiency (%)
ZSW	Co-evaporation	CdS	ZnO, ZnO:Al	20.3 [5]
NREL	Co-evaporation	CdS	ZnO	19.9 [6]
AGU	MBE*	ZnS	ZnO:Al	18.6 [7]

MBE*: Molecular beam epitaxy.

1.3 CIGS Solar Cells Buffer Layer

Buffer layer is indispensable in high-efficient CIGS thin-film solar cells. The functions of buffer layer are listed below.

1) **Match band-gap between window layer and absorber layer**
2) **Protect absorber layer from ion bombardment**
3) **Provide the p-n junctions**

In CIGS solar cells, ZnO is commonly used as window materials. The band-gap of ZnO is about 3.2 eV, and the band-gap of CIGS absorber layer is about 1.0 to 1.7 eV. If the ZnO is deposited on CIGS, the large band offset in CIGS/ZnO interface may cause severe carriers' recombination which can dramatically decrease cell efficiency. In order to reduce the carriers' recombination, the addition of the CdS as buffer layer is needed.

Buffer layer can protect absorber layer from the damage by sputtering which is the most applied technique in depositing window layer ZnO. During the sputtering, strong-energy argon (Ar) plasma ions will destroy the surface of CIGS absorber layer by ion bombardment. Therefore, the addition of buffer layer is used to protect the surface of absorber layer.

The formation of p-n junctions is important in solar cells. When electrons in solar cells are excited under the illumination, these electrons will be driven to the electrodes by the build-in electric field caused by p-n junctions. The purpose of buffer layer is to yield the n-type semiconductor accompanying with the p-type CIGS.

High-active CdS is commonly utilized in high-efficient CIGS solar cells because CdS can achieve thin and high-coverage film. The band-gap of CdS is about 2.4 eV which means CdS can also provide desirable matching between ZnO and CIGS. However, optical loss by the wavelength below 520 nm of sunlight from lower band-gap and Cd toxicity are the issues. Therefore, the investigation of Cd-free buffer materials with higher band-gap is recommended.

Showa Shell investigated ZnS deposited by chemical bath deposition (CBD) method as Cd-free buffer materials, as well as the cells efficiency in module achieved 12.5% [8-9]. CBD-ZnS has higher optical transmission in short wavelength regions of sunlight because the band-gap of CBD-ZnS is much larger than the band-gap of CBD-CdS. The quantum efficiency (QE) of CBD-ZnS and CBD-CdS compared by Nakada Group is shown in Fig. 4 [10]. The quantum efficiency of CBD-ZnS below the blue light region is higher than CBD-CdS, indicating the advantage of CBD-ZnS.

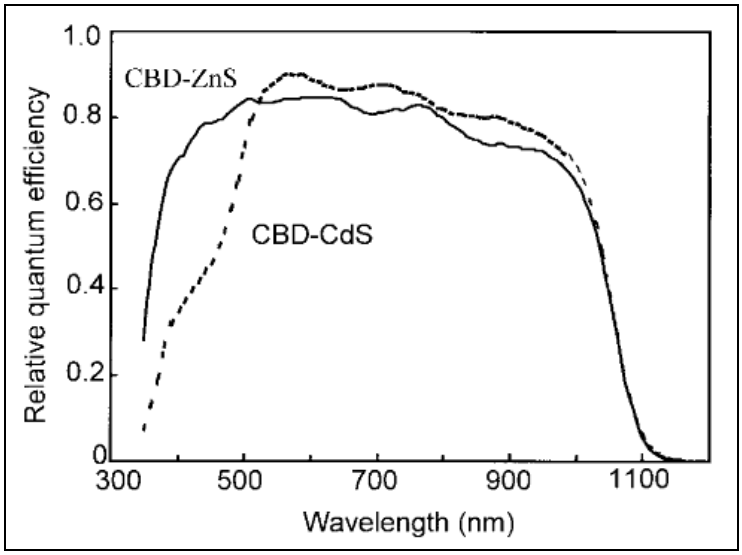

Fig. 4 Comparison of relative QE between CBD-ZnS and CBD-CdS

Indium sulfide (In_2S_3) also provides the feasibility of replacing CdS. To obtain high performance, In_2S_3 is fabricated by CBD and atomic layer deposition (ALD). CBD-In_2S_3 deposited in CIGS solar cells by Prof. Dimitri Hariskos from ZSW achieved 15.7% in efficiency [11]. Cells efficiency of In_2S_3 deposited with ALD on CIGS by Prof. Naghavi from Centre National de Recherche Scientifique, Laboratoire d'Electrochimie et de Chimie (LECA-CNRS), France, was 16.4% [12].

So far, although CBD-ZnS and ALD-In_2S_3 are still not competitive with CBD-CdS, many research institutes and industries have dedicated to investigate ZnS and In_2S_3 due to their potential of better optical transmission below the short-wavelength region and without the Cd utilization. The simple comparisons of buffer materials fabricated by the three research institutions are listed in Table 2.

Table 2 Comparisons of three buffer materials

Buffer material	Deposition method	Institutes	Efficiency (%)	Features
CdS	CBD	ZSW	20.3 [5]	High-efficiency
ZnS	CBD	AGU	18.6 [7]	QE response
In_2S_3	ALD	LECA-CNRS	16.4 [12]	Stable

1.4 Motivation

CIGS is one of the potential materials for thin-film solar cells due to its high absorption coefficient and direct band-gap, so many research institutes work for bringing CIGS solar cells to mass production. During the fabrication, buffer layers deposited on CIGS film by non-vacuum CBD were reported to show better performance because CBD method could provide the benefits such as easy to scale-up, low cost, and short processing time. Furthermore, consider of environmental issues, optical transmittance, and performance in cells efficiency, the ZnS buffer layer deposited by CBD method is preferred.

However, it is difficult to accurately control the compound reaction in CBD method because CBD method is a non-vacuum process. The appearance of zinc hydroxide ($Zn(OH)_2$) in ZnS films cannot be avoided in CBD process. Also, the relatively low activity of ZnS is hard to form thin and well-coverage films. Therefore, there are some issues in accomplishing the balance between stable fabrication process, suitable stoichiometric ratio, well coverage properties, and thin-thickness in CBD-ZnS. In this thesis, some methods will be proposed to improve these issues.

1.5 Organization

In this thesis, “The zinc sulfide buffer layer fabrication using chemical bath deposition processes in Cu(In,Ga)Se_2 thin film solar cells” will be discussed. The structure is shown as follows. The principle of photovoltaic effect, CIGS fabrication, and the characteristics of fabricating technique are presented in **Chapter 2.** In **Chapter 3**, the fabrication processes, the fabrication facilities, and the measurements are explained in detail. Results and discussions of ZnS films on the CIGS/Mo-coated substrate are described in **Chapter 4**. Finally, the conclusion and future works are presented in **Chapter 5**.

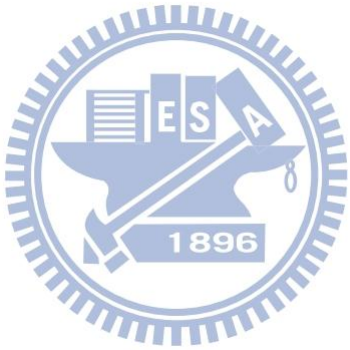

Chapter 2 CIGS Solar Cells

The principle of photovoltaic effect in solar cells will be presented. Four fabrication techniques will be introduced, including sputtering, thermal evaporation, annealing, and chemical bath deposition.

2.1 Principle of Photovoltaic Effect

The concept of discrete portions of the light's energy was firstly introduced by Max Planck and further confirmed by Albert Einstein who proposed that light can be regard as the composition of packets of photons. The photon energy E_{photon} is equal to the product of h and ν, where h is the Planck's constant and ν is the frequency of light. The frequency ν (s^{-1}) is related to the wavelength λ (m) through the speed of light c (m/s) by $\nu = c/\lambda$ and the relationship is written as equation 2-1 as shown below.

$$E_{photon} = h\nu = hc/\lambda \qquad \text{Eq. 2-1}$$

The principle of solar cells was based on the photovoltaic effect and the effect was proposed by Albert Einstein in 1939 [13]. In a semiconductor material, the minimum energy required for generating a free electron is the energy E_g, where E_g is the energy between the valence band and conduction band. When the semiconductor material is illuminated, the material absorbs the incoming energy which is larger than the band-gap of the semiconductor material. The photon energy of an incoming photo excites an electron from the valence band to the conduction band and leaves behind a hole in valence band. A schematic of photovoltaic effect in the semiconductors under illumination is illustrated in Fig. 5.

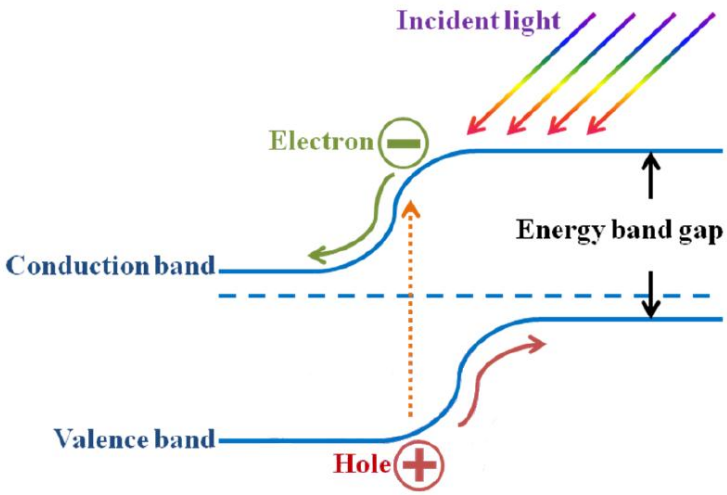

Fig. 5 Schematic of photovoltaic effect in semiconductors

When the p-n junctions formed by contacting the p-type and n-type semiconductors is illuminated by incident light, the excited carriers are generated and driven by the build-in electric field between p-n junctions. Eventually, the light current will generate if the p-n junction is connected to an external circuit.

The generation of short circuit photocurrent is dependent on the incident photons. The connection between short circuit photocurrent and incident photons is shown in the following equation

$$J_{sc} = q \int b_s(E) Q.E.(E) dE \qquad \text{Eq. 2-2}$$

where J_{sc} is named as the short circuit current density, q is the electronic charge, $b_s(E)$ is the incident spectral photon flux density, and Q.E.(E) is the quantum efficiency of incident photon carrying with energy E.

Except the photocurrent, there is another current delivers the opposite direction to the photocurrent because the p-n junctions inside the semiconductor can be treated as the p-n diode. This reverse current is called the dark current and it is developed by the potential difference between the terminals of the diode. The dark current density can be described in equation 2-3.

$$J_{dark}(V) = J_o(e^{qV/AK_BT} - 1) \qquad \text{Eq. 2-3}$$

Where J_0 is the reversed saturation current, q is the electronic charge, V is the bias voltage without illumination, A is the ideality factor of diode which is decided by materials, K_B is Boltzmann's constant, and T is absolute temperature (k).

Since the short circuit current and the dark current are in the opposite direction, the net current density $J(V)$ in the solar cells is defined as

$$J(V) = J_{sc} - J_{dark}(V) \qquad \text{Eq. 2-4}$$

Bringing equation 2-3 into equation 2-4, equation 2-4 can be simplified to

$$J(V) = J_{sc} - J_0(e^{qV/AK_BT} - 1) \qquad \text{Eq. 2-5}$$

When $J(V)$ is equal to zero, the open-circuit voltage V_{oc} can be obtained from equation 2-5

$$V_{oc} = \frac{AK_BT}{q} ln \left(\frac{J_{sc}}{J_o} + 1 \right) \qquad \text{Eq. 2-6}$$

The current voltage characteristic of solar cell is illustrated in Fig. 6, the operating region works in the range of $0 < J < J_{sc}$ and $0 < V < V_{oc}$ of solar cell.

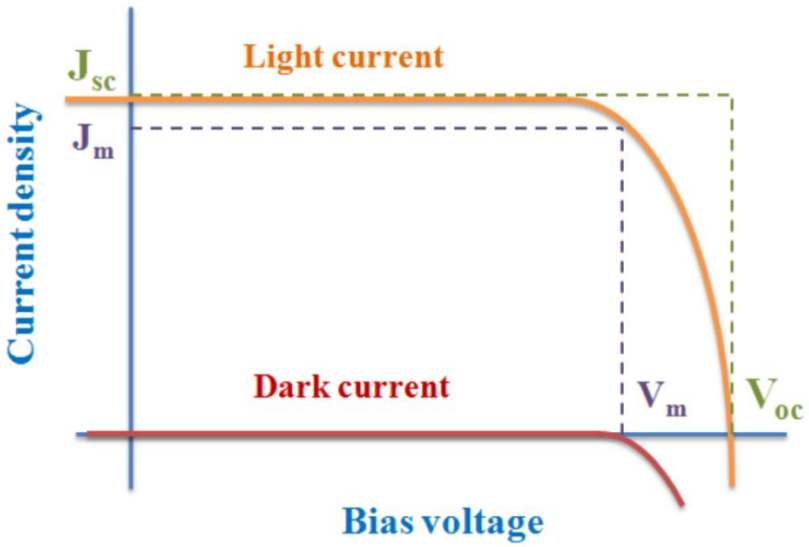

Fig. 6 Current voltage characteristic of the solar cell

The power density P is the product of the current density J and the bias voltage V. The maximum power density is defined by the product of the current density J_m and the bias voltage V_m. The equation is given by

$$P_m = J_m V_m \qquad \text{Eq. 2-7}$$

The fill factor (FF) which is used for evaluating the performance of solar device is defined in equation 2-8.

$$FF = \frac{P_m}{J_{sc} V_{oc}} = \frac{J_m V_m}{J_{sc} V_{oc}} \qquad \text{Eq. 2-8}$$

The conversion efficiency η of a solar device is further acquired by the maximum power density P_m over power density P_s of the incident light.

$$\eta = \frac{P_m}{P_s} = \frac{J_m V_m}{P_s} = \frac{J_{sc} V_{oc} FF}{P_s} \qquad \text{Eq. 2-9}$$

Apparently, the efficiency η can be described by Jsc, Voc, as well as FF. These four characteristics η, Jsc, Voc, and FF are usually used for appearing the performance of solar cells. Typical values of the performance characteristics for the most advanced CIGS and other thin-film solar cells are listed in Table 3 [3].

Table 3 The performance characteristics in three kinds of solar cells

Classification	Efficiency (%)	Area (cm^2)	Voc (V)	Jsc (mA/cm^2)	FF (%)
CIGS	20.3 ± 0.6	0.502 (ap*)	0.740	35.4	77.5
CdTe	16.7 ± 0.5	1.032 (ap*)	0.845	26.1	75.5
a-Si:H	12.5 ± 0.7	0.27 (da*)	2.010	9.11	68.4

ap*: aperture area

da*: designated illumination area

2.2 CIGS Fabrication in each layer

2.2.1 Substrate

It is very important to choice substrates used in CIGS solar cells since the substrates need to be stable during the fabrication. The substrates should be chemically-inert from the selenization process and thermally-stable from the high-temperature annealing in the range of 400 to 600 ℃. So far, plate glass substrates are adopted for the application.

Soda-lime glass is usually used as the substrates in CIGS solar cells because of the feasible price and sodium (Na) diffusion from SLG to CIGS absorber layer, where Na diffusion can improve the structural and electrical properties. It was reported that the CIGS solar cells deposited on the SLG (Na = 0.1 at %) were found to have higher conversion efficiencies than the one prepared on the borosilicate substrates [14-15].

2.2.2 Back Contact Layer

The back contact layer is the back electrode of the CIGS solar cells. Several materials were reported to be the contact metal such as tungsten (W), molybdenum (Mo), and Titanium (Ti) [16-17]. Among the metals, Mo was chosen typically as back metal contact. Mo, the historical back contact material for CIGS solar cells, achieved well performance with most favorable electricity, optical properties, and the inertness from the highly corrosive process. Sputtering is the common deposition technique for Mo layer. To obtain the Mo film with low resistivity and good adhesion, two stacking layers are applied by sputtering the first layer with good adhesion in high working pressure and the second layer with low resistivity in low pressure condition.

In addition, during the CIGS formation procedure at high temperature, Mo may interact with active selenium (Se) to form an extremely thin molybdenum diselenide ($MoSe_2$) layer in the interface between Mo and CIGS. The formation of $MoSe_2$ was reported to benefit the solar device performance because the appearance of $MoSe_2$ resulted in the ohmic contact which was favorable for current transferred [18-19]. Moreover, $MoSe_2$ could improve the adhesion between CIGS and Mo [20].

2.2.3 CIGS Absorber Layer

CIGS absorber layer can be fabricated by both vacuum and non-vacuum processes. In general, the absorber formed by vacuum processes reveals higher efficiency than that of non-vacuum processes. The vacuum processes of the co-evaporation method and the selenization process of precursors will be introduced in the following.

Co-evaporation

Co-evaporation is the best method among the CIGS deposition techniques, especially for laboratory-scale devices because of the flexibility of the Cu, In, Ga, and Se flux in evaporation process. The latest world record of cells efficiency in CIGS solar cells has achieved 20.3% by using this co-evaporation method. The typical co-evaporation facility for fabricating CIGS thin films is shown in Fig. 7.

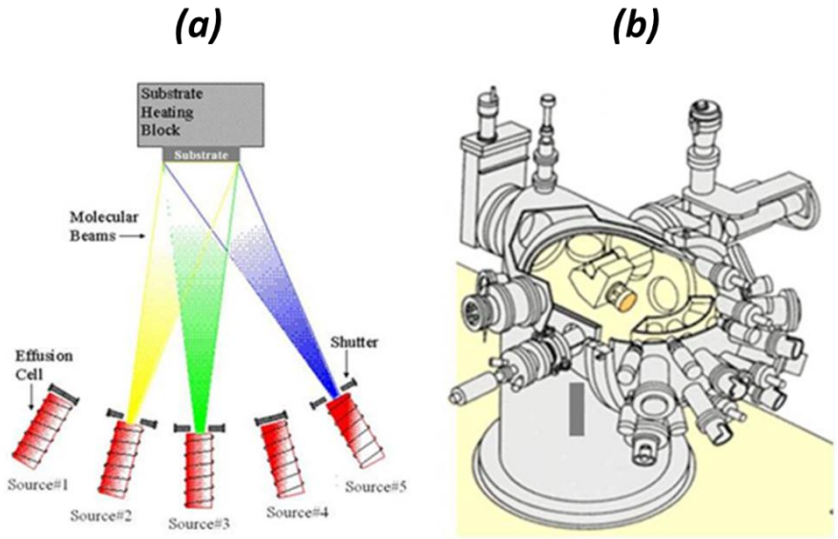

Fig. 7 Schematic of (a) co-evaporation principle and (b) cavity structure

The most successful modification of the co-evaporation process was called three-stage process as shown in Fig. 8 [21]. In the first stage, the sources of In, Ga, and Se were evaporated simultaneously on the substrate heated at 350 ℃. Then the source of Cu and Se were evaporated in the second stage at 550 ℃. At the end of the three-stage process, the source of In, Ga, and Se were evaporated simultaneously again at 550 ℃ to ensure the variations of the Ga/In and Cu/(In+Ga) ratio for graded band-gap through the film [22-23].

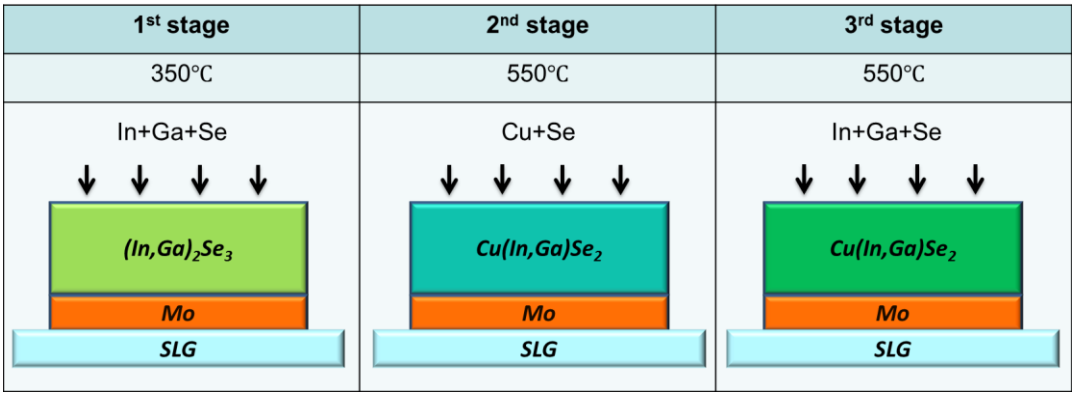

Fig. 8 Three-stage process: 1st stage: In, Ga, and Se co-evaporation at 350 ℃, 2nd stage: Cu and Se co-evaporation at 550 ℃, and 3rd stage: In, Ga, and Se co-evaporation at 550 ℃

Even through the CIGS film fabricated by three-stage co-evaporation process is realized with the smooth, dense, and well-controlled film, the capability for the large-scale application in commercial use should be concerned due to the uniformity through the module panel.

Selenization of Metallic Precursors

Selenization process with Cu-In-Ga (CIG) metallic precursor is another method to fabricate CIGS thin film. The first step is to stack CIG precursor on Mo-coated substrate and then the second step is to selenize the CIG precursor with the use of hydrogen selenide (H_2Se) or Se vapor. The selenization process has the advantages of manufacturing in large-scale CIGS modules compared with co-evaporation process. Many researchers provided the cell efficiency over 10% by selenizing the metallic precursors in H_2Se or by rapid thermal processing (RTP) of stacked precursors in the Se atmosphere [24-26]. The possibilities for film formation by different reactive processes is illustrated Fig. 9.

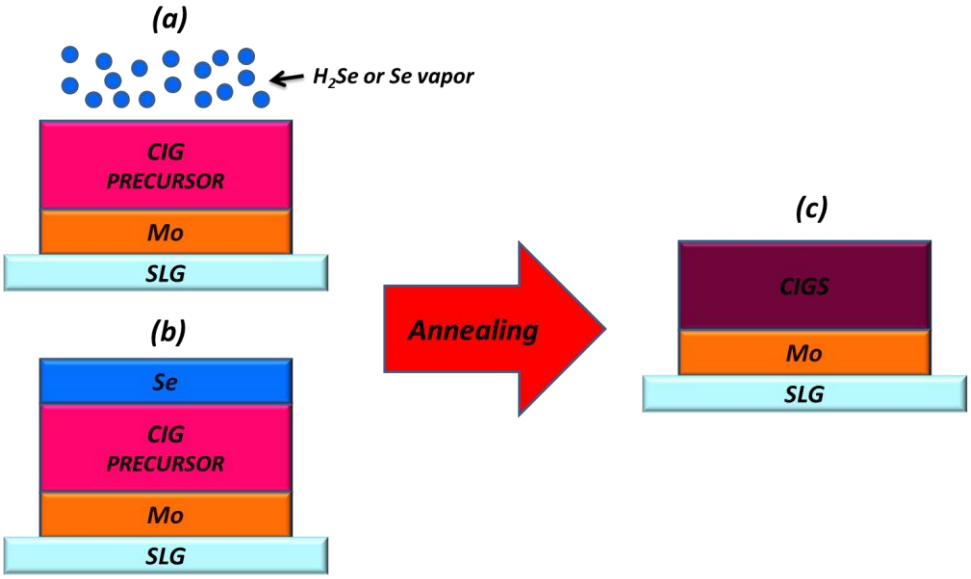

Fig. 9 Reaction process of (a) Se/H_2Se vapor, (b) Se solid layer, and (c) CIGS formation

2.2.4 Buffer Layer

The buffer material acts as a matching layer both electrically and optically between the absorber layer and window layer. So far, variety kinds of buffer materials were investigated for the better performance and fabricated by either vacuum or non-vacuum process.

The method to deposit the buffer layer on CIGS absorber layer is mainly employed by non-vacuum CBD method in high-efficient solar cells. CBD method were reported to show better performance than any other vacuum process methods because CBD process can provide the benefits such as good film coverage, low cost, and short processing time.

The CdS films deposited by CBD method are widely used as an interfacial layer of the high efficiency CIGS thin-film solar cells. Recently, several research groups report that the diffusion of Cd into the CIGS absorber can form buried p-n junctions inside the absorber [27]. However, the used of Cd is concerned due to the environment issues. Consider of environmental protection, thin film ZnS is preferred as the substitution for CdS. The more detail about CBD-ZnS will be discussed in Chapters 3 and 4.

2.2.5 Window Layer

Window layer, as the name implied, behaves as the function of the window for the light passing through. The objectives of window layer in CIGS solar cells must have:

1) **The minimized light absorption**

2) **Low resistivity for carriers transportation**

In order to minimize the absorption and to lower the ohmic losses in the window

layer, the band-gap of the chosen materials should be relatively wider. To form hetero-junctions, this window layer should contain n-doped materials. Transparent conducting oxides (TCO) which are provided with well-conductivity and high-transparent agree with the criteria. Indium tin oxide (ITO) is a well-known TCO in flat-panel industries and solar technologies. However, the available ITO usage is reduced due to the In limitation, so other alternatives are being studied. One of the potential alternatives in CIGS solar devices is ZnO:Al because Al and ZnO are easily-obtained on Earth.

An ordinary deposition technique for the window layer is fabricated by sputtering. As shown in Fig. 10, before sputtering ZnO:Al window layer on buffer layer, a high resistivity intrinsic ZnO (i-ZnO) was sputtered to prevent the shunt-path from ZnO:Al to Mo. Other benefits like increasing open-circuit voltage and fill factor of the device are also significantly dependent on involving the high resistivity i-ZnO in CIGS solar devices.

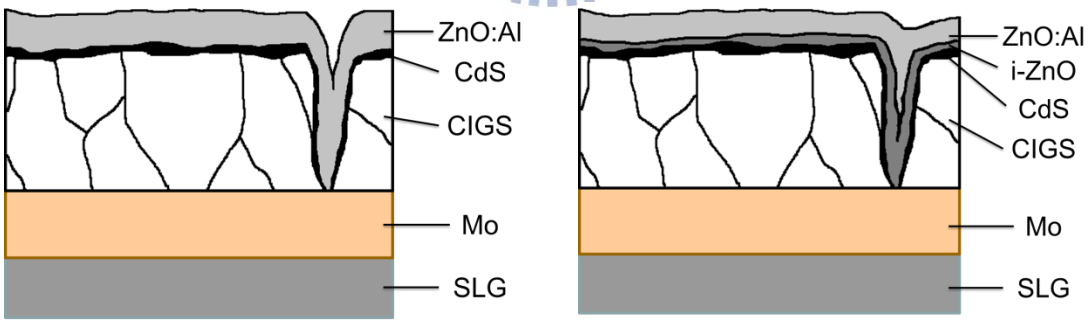

Fig. 10 The shunt-path prevention by sputtering i-ZnO layer

Since this deposition of window layer is almost the last step in the CIGS solar cells fabrication, the working power, pressure, and temperature during or after sputtering process have to be controlled carefully for preventing the damage to front layers.

2.3 Fabricating Technique

The fabrication techniques: sputtering system, thermal evaporation system, annealing process, and chemical bath deposition used in this thesis will be illustrated.

2.3.1 Sputtering System

Sputtering causes particles ejection by momentum transfer in the high vacuum level ($10^{-5} \sim 10^{-8}$ Torr). The momentum transfer is caused by striking energetic ions or neutral atoms on the surface of a solid target.

A schematic of the sputtering process is shown in Fig. 11. In general, sputtering system consists of a power supply, vacuum atmosphere, working gas, vacuum pumps, targets, and a sample holder.

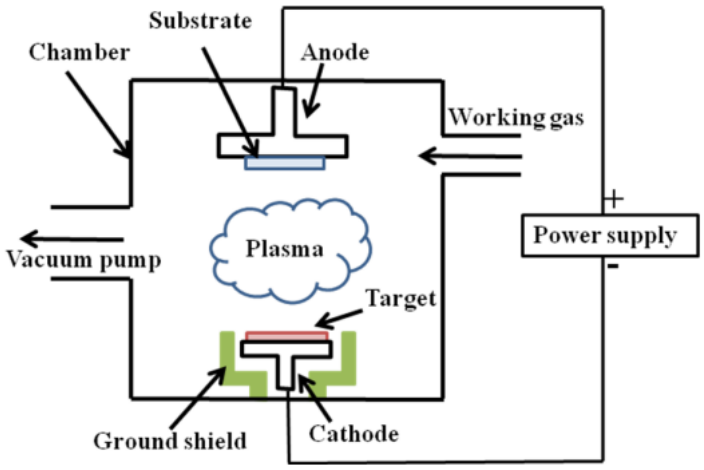

Fig. 11 Schematic of sputtering system

In a typical sputtering process, the chamber is evacuated to high vacuum atmosphere before sputtering. Then the Ar working gas flows into the chamber until the working pressure in the chamber achieves 10^{-3} Torr level. The target is then biased by a direct current (DC) or radio frequency (RF) on negative electric potential

to produce the plasma between target and ground shield. The energetic ions in the plasma sustain the glow-discharge situation. The positively charged ions are driven by the potential gradient across the chamber and are accelerated to strike the surface of the target to dislodge particles of the target. The ejected particles then travel through the chamber and finally deposit onto the substrate.

2.3.2 Evaporation System

The system of evaporation deposition is to heat a boat with material pellets to sufficiently high temperature under vacuum so that particles are liberated from the boat and the particles travel through the vacuum to deposit onto the substrate. This method includes three characteristics:

1) **The desirable materials transfer from solid phase to vapor phase**
2) **Transportation from source to substrate**
3) **Nucleation and growth of film on the sample surface**

A schematic of evaporation system is shown in Fig. 12. The evaporation system consists of a chamber, vacuum pumps, material sources, a heating system, and a sample holder.

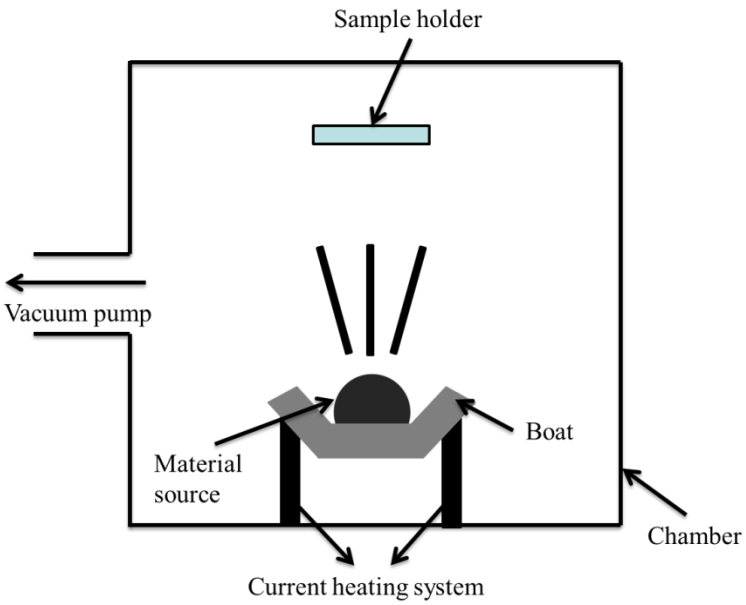

Fig. 12 Schematic of evaporation system

High vacuum in the chamber is required for reducing the residual gas impurity levels, maximizing the molecule absorption rate onto the substrate surface, and decreasing the amount of unnecessary gas phase collisions.

2.3.3 Annealing Process

Annealing is often applied in metallurgy or materials engineering fabrication process. The purpose of annealing is to improve thin-film crystallization and release the internal residual stress.

A schematic of annealing system is shown in Fig. 13. The annealing system consists of a chamber, vacuum pumps, working gas, heating sources, and a sample holder.

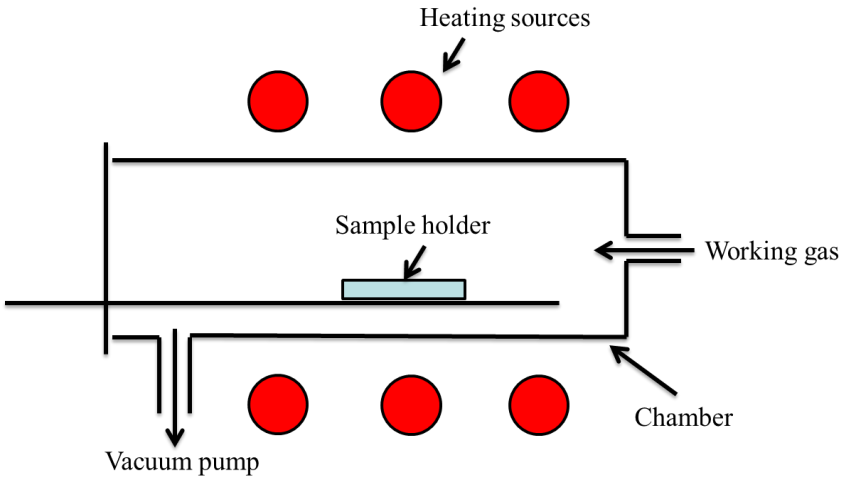

Fig. 13 Schematic of annealing system

To enhance the crystalline structure after fabrication process, the annealing process is required. Annealing process is a heating process containing three temperature steps: heating, maintaining, and cooling. In the heating step, the temperature must reach the materials recrystallization temperature. The temperature is maintained for a period of time to provide energy for recrystallization and grain growth. Cooling must be stable and slow to prevent the inherent-stress damage.

2.3.4 Chemical Bath Deposition

Chemical bath deposition, classified by the growth mechanism, can be divided into two main types: ion by ion collision and cluster reaction. For the mechanism of ion by ion growth, a high-degree of supersaturation is needed to nucleate. The ion-by-ion mechanism introduces the heterogeneous nucleation right on the surface, such as substrates or vessel walls, to form the films. Cluster reaction, also named as hydroxide mechanism, is the nucleation of metal chalcogenide. In this mechanism, the metal hydroxide film forms on the surface of substrates at the beginning, and then hydroxyl is substituted by chalcogenide. The continuous of metal hydroxide

deposition and chalcogenide substitution create the buffer films.

The detail of both mechanisms is shown in Fig. 14, where the ZnS and $Zn(OH)_2$ are employed to illustrate the growth mechanisms.

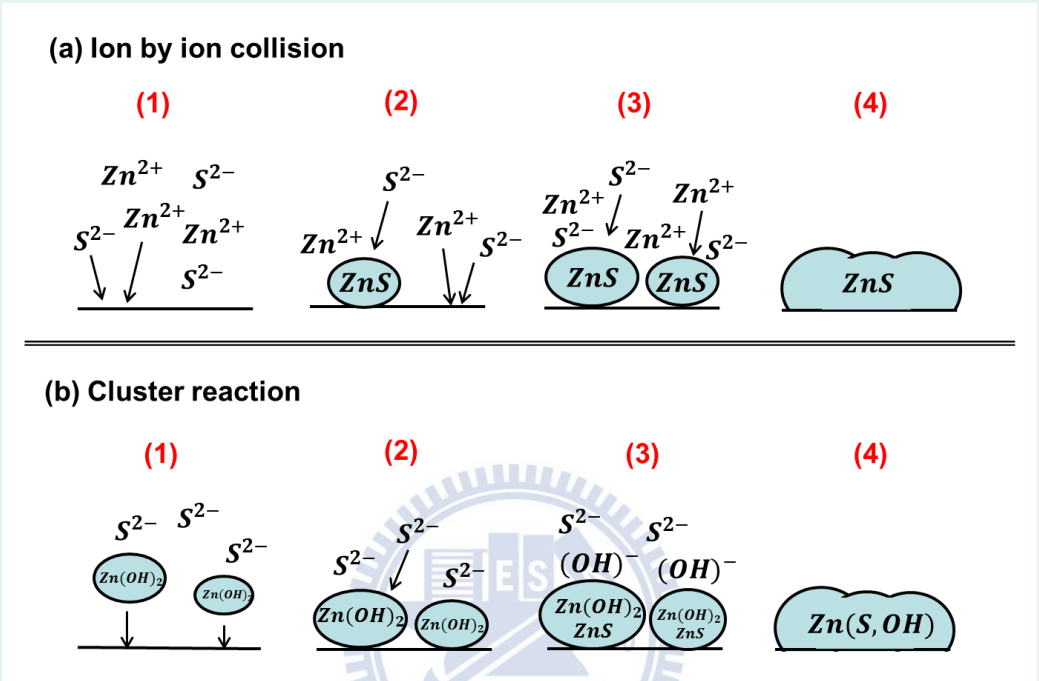

Fig. 14 Schematic of mechanisms (a) Ion by ion collision and (b) Cluster reaction

The ion-by-ion collision contains four steps as shown in Fig. 14 (a):

(1) S and Zn ions diffuse onto the substrate

(2) The ZnS nuclei forms

(3) Growth and aggregation of the ZnS nuclei

(4) ZnS forms as the film

The cluster reaction also includes four steps as shown in Fig. 14 (b):

(1) Diffusion of $Zn(OH)_2$ colloids to the substrate

(2) $Zn(OH)_2$ colloids adhere to the substrate

(3) Hydroxide is replaced by sulphide at the surface

(4) The film Zn(S,OH) forms

Ammonia which provides the complex ions and hydroxyl is added in the CBD process to control the amount of Zn ions by Zn-complexes and the pH value. By adjusting the amount of Zn ions and the pH value, the rates of reaction can be controlled to deposit favorable films.

During the deposition, the solution is heated by a heat plate connected with a temperature controller which is to maintain the stationary temperature in the region of 60 to 90 ℃. A magnetic bar is kept in stirring to retain the solution uniformity.

After the deposition, post-treatment like ultrasonic cleaning and baking of deposited films is needed to enhance the film properties. The ultrasonic cleaning removes the loose particles on the films surface and the baking eliminates the moisture produced from aqueous solution.

The solubility product constant (K_{sp}) is an important factor in chemical bath reaction. Consider the reaction of a compound AB dissolves in solution,

$$AB_{(s)} \rightleftarrows A^{+}_{(aq)} + B^{-}_{(aq)}$$

K_{sp} is defined as the product of a constant k, $A^{+}_{(aq)}$, and $B^{-}_{(aq)}$ concentration in equilibrium,

$$K_{sp} = \mathrm{k}\left[A^{+}_{(aq)}\right] \times \left[B^{-}_{(aq)}\right] \qquad \text{(equilibrium)}$$

The constant k is relative to the absolute temperature. For a non-equilibrium reaction of the compound AB dissolves in solution, J is defined as the product of a constant k, $A^{+}_{(aq)}$, and $B^{-}_{(aq)}$ concentration in this non-equilibrium condition.

$$\mathrm{J} = \mathrm{k}\left[A^{+}_{(aq)}\right] \times \left[B^{-}_{(aq)}\right] \quad \text{(non-equilibrium)}$$

When J $>$ K_{sp}, the precipitation occurs. When J $= K_{sp}$, the reaction is in equilibrium. When J $<$ K_{sp}, the compound dissolves. The K_{sp} at room-temperature of common products in CBD-CdS and CBD-ZnS are shown in Fig.15 and listed in Table 4. Owing to a small K_{sp} value of the ZnS film, the deposition rate and the growth mechanism of the thin film must be controlled by the complex agents such as ammonia, hydrazine, and ethylenediamine tetra-acetate (EDTA).

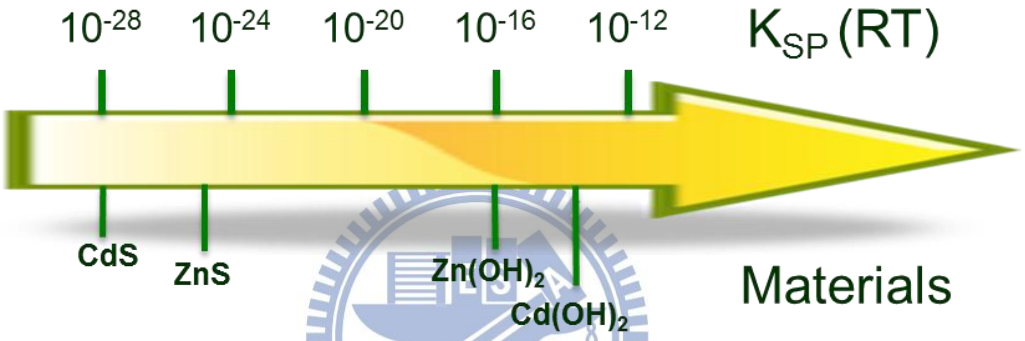

Fig. 15 Comparison of common products in CBD

Table 4 The K_{sp} (RT) of several materials [28]

Materials	K_{sp} (RT)
CdS	1×10^{-28}
$Cd(OH)_2$	1×10^{-14}
ZnS	3×10^{-25}
$Zn(OH)_2$	1×10^{-16}

Chapter 3 Experiment

A deposition system in National Chiao-Tung University (NCTU) will be illustrated, including a sputtering chamber, a selenization chamber, and an experimental setup for fabricating the ZnS film on CIGS/Mo/SLG. Analytical equipments such as scanning electron microscope (SEM), energy dispersive X-ray spectrometer (EDX), UV-VIS spectrometer, and MATLAB Numerical Analysis will be illustrated.

3.1 CIGS Deposition System

To deposit CIGS thin film, a self-designed CIGS deposition system was used in this thesis. This deposition system consisted of a sputtering and a selenization chamber. A load-lock chamber was connected between the sputtering and the selenization chamber so that the sample could be maintained in a relatively clean environment during the different fabrication process. A schematic of the CIGS deposition system is shown in Fig. 16.

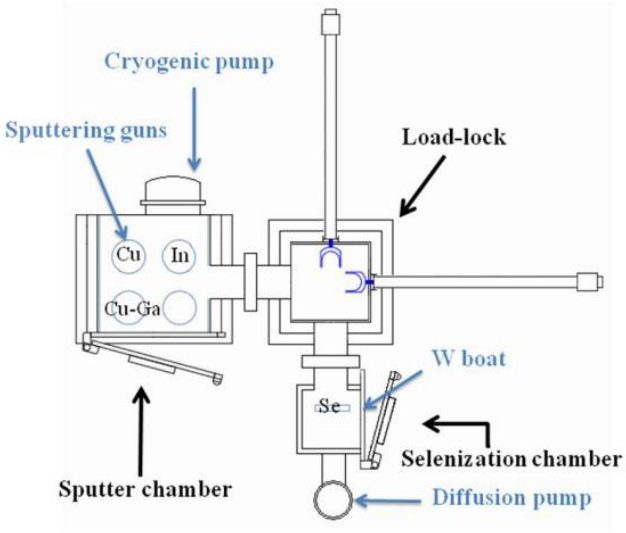

Fig. 16 Schematic of CIGS deposition system in NCTU

Photographs of the sputtering system and the selenization system are shown in Figs. 17 and 18, respectively.

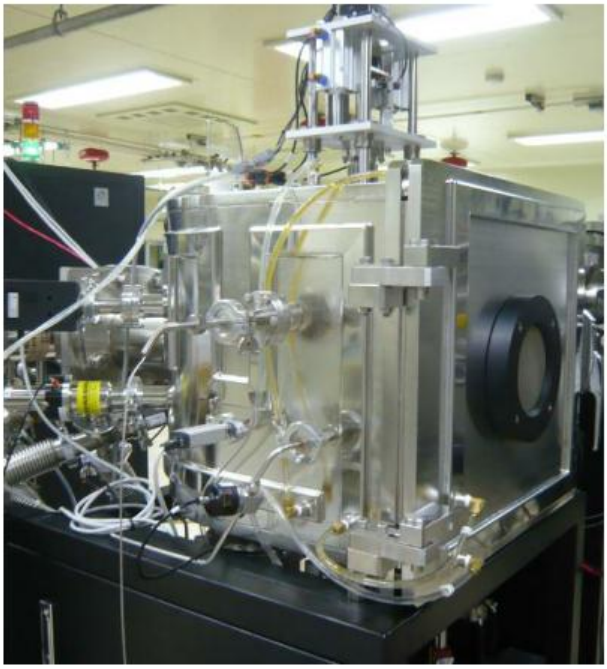

Fig. 17 Photograph of the sputtering system

Fig. 18 Photograph of the selenization system

In order to achieve the high vacuum level in the sputtering system, a mechanical pump and a cryogenic pump were set up. The mechanical pump was an oil-sealed rotary pump, which was used to establish the necessary fore-vacuum value for the cryogenic pump. It could bring the pressure from atmosphere to around 5×10^{-2} Torr. Cryogenic pump was based on the principle of cold trap. Over several periods of removal and entrapment by freezing the molecules on the cooled surface, the pressure in the chamber was pumped down. In this system, the based vacuum was 7×10^{-7} Torr.

The 3-inch target with a smooth surface and symmetrical disk-shape were made of the materials for the deposition. In this thesis, metallic targets like Mo, Cu, and In, as well as compound targets like Cu-Ga, intrinsic ZnO, and ZnO:Al were used in cell fabrication.

To attain a high vacuum level in selenization system, two pumps were used in fabrication process: a rotary pump and a diffusion pump. Before launching the evacuation for requisite vacuum level by the diffusion pump, the rotary pump was served to assist the diffusion pump by constantly removing gas molecules. During the operation of the diffusion pump, the oil was heated to around 200 ℃ which percolated at high velocity through a series of baffle plates to remove gas molecules. After the operation, the desirable high vacuum level was acquired. An issue has to be concerned that the back streaming of oil from the heated diffusion pump may diffuse into the processing chamber and contaminate the sample.

The selenization system was composed of the evaporation and annealing process in the same chamber in order to retain the Se-vapor in annealing process. During the annealing process, the retention Se-vapor would contribute to the CIGS grain growth.

In this thesis, Se pellets as the source were placed in a thermally heated tungsten boat and were evaporated by the thermal evaporation. Thermodynamically, the partial

pressure of the source material in the gas phase had to be greater than in the solid phase in order to deposit Se on the substrate.

After the evaporation of elemental Se on the metallic precursors, the annealing process in the Se-containing atmosphere was applied in the same chamber and the films were heated by halogen lamps. The annealing process with Se-vapor was a heat treatment that involves three steps: heating, maintaining for a period, and cooling. After the selenization process, the recrystallization of Cu-In-Ga precursor with Se layer would form CIGS polycrystalline. The chemical as well as physical properties of precursors might change after the conditions on selenization process such as elemental diffusion.

3.2 The Process of CIGS Fabrication

In this section, the CIGS fabrication process will be introduced. The buffer material ZnS deposited on SLG and CIGS/Mo/SLG substrates will be investigated.

3.2.1 Substrate Cleaning

In order to remove the undesired particles and contaminations on the SLG substrate, the SLG is cleaned as follows:

(a) Clean the SLG substrate by deionized (DI) water

(b) Clean the SLG with detergent and then wash out the detergent

(c) Place the SLG on the teflon holder, and put the holder into a container with acetone. Remove the organic contamination by the ultrasonic cleaning for 20 minutes.

(d) Place the SLG into another container with isopropanol (IPA). Remove acetone by the ultrasonic cleaning in 20 minutes.

(e) Place the SLG into a third container with DI water. Apply the ultrasonic

cleaning in 20 minutes.

(f) Use nitrogen jet to purge and dry the SLG.

(g) Put the SLG on a hot plate with 150 ^{o}C for 30 minutes to remove surface moisture.

3.2.2 Back Contact Metal Deposition

The back contact metal Mo was deposited on the cleaned SLG substrate by DC magnetron sputtering with thickness around 0.8 μm. The sputtering chamber was pumped down to the base vacuum of 7×10^{-7} Torr. The working pressures were set to be between 10^{-3} and 1.5×10^{-2} Torr, and the powers of the sputtering gun were set up between 50 and 150 W. During the sputtering, the sample holder rotated with a rotating rate of 10 revolutions per minute (rpm).

3.2.3 CIGS Absorber Deposition

The preparation of CIGS absorber can be divided into two parts: deposition of metallic precursors and selenization process.

Deposition of Metallic Precursors

The CIG precursors were deposited on the Mo-coated substrate by DC magnetron sputtering. During the sputtering, the sputtering chamber was pumped down to a base pressure of 7×10^{-7} Torr. The chamber pressure was set to be 5×10^{-3} Torr by filing with Ar gas, and the power of the sputtering gun was set to be 50 W on a 3-inch target. The sample holder rotated at a rotating rate of 10 rpm. The deposition was started at room temperature.

The deposition of precursors was stacked in two ways: sequential and simultaneous deposition. The stacking methods by the sequential and simultaneous

deposition might affect the CIGS surface morphology, vertical composition, and the crystalline quality of the films after selenization. In addition, to obtain the desirable composition of film, the film deposition was accomplished by sequentially depositing In thin layers and then simultaneously depositing Cu-Ga and In layers. The power applied on Cu and Cu-Ga targets was adjusted while the power applied on In target was fixed.

Selenization Process

To incorporate Se into the precursors, Se might be evaporated onto the surface of precursors in advance and followed by an annealing process in the Se-containing atmosphere. The selenization chamber was pumped down to a base vacuum of 10^{-6} Torr. During the selenization, the sample holder rotated at a rotating rate of 10 rpm. The annealing temperatures were set between 350 and 550 ℃.

Selenization was a key process that affects the resulting adhesion, composition, orientation, and phase purity of films. Se was usually supplied excessively to assure the complete formation of selenides (CIGS, In_2Se_3, or Cu_2Se) with Cu-In-Ga precursors since elemental Se might escape from surface of the sample due to the low vaporization point of Se. Therefore, the flux of Se source for evaporation and the annealing temperature should be carefully controlled.

3.2.4 Chemical Bath Deposition

To deposit ZnS films by CBD method in this thesis, the solution consisted of zinc sulfate ($ZnSO_4$) as a source of zinc (mole concentrations ranged from 0.02 M to 0.6 M) and thiourea ($CS(NH_2)_2$) as a source of sulfide (mole concentrations ranged from 0.2 M to 0.8 M). Ammonia was added into the solution to provide an alkaline environment and adjust pH level around 9 to 11. The composition of solution, the

hydrolysis reaction of $ZnSO_4$, $CS(NH_2)_2$, ammonia, and part of reaction equations are listed in Tables 5 and 6, respectively.

Table 5 The compositions of CBD solution

$ZnSO_4$ (M)	0.02 ~ 0.6
$CS(NH_2)_2$ (M)	0.2 ~ 0.8
NH_3 (M)	2 ~ 6
pH	9 ~ 11
Temp. (℃)	60 ~ 90

Table 6 The hydrolysis reaction and main reaction equations in CBD

$ZnSO_4 \leftrightarrows Zn^{2+} + SO_4^{2-}$	(1)
$NH_2CSNH_2 + 2OH^- \leftrightarrows S^{2-} + CH_2N_2 + 2H_2O$	(2)
$NH_4^+ + OH^- \leftrightarrows NH_3 + H_2O$	(3)
$Zn^{2+} + S^{2-} \leftrightarrows ZnS(s)$	(4)
$Zn^{2+} + 2OH^- \leftrightarrows Zn(OH)_2(s)$	(5)
$Zn^{2+} + 4NH_3 \leftrightarrows Zn(NH_3)_4^{2+}$	(6)
$Zn(NH_3)_4^{2+} + 2OH^- \leftrightarrows Zn(OH)_2(s) + 4NH_3$	(7)
$Zn(OH)_2(s) + S^{2-} \leftrightarrows ZnS(s) + 2OH^-$	(8)

The solution temperature controlled by temperature controller was set up at 60 to 90 ℃. A magnetic bar was kept in stirring to maintain the solution uniformity. To investigate the ZnS films properties, ZnS was deposited on both SLG and CIGS/Mo/SLG substrates. After the deposition, each film was cleaned by ultrasonic

cleaning in deionized water to remove the loose ZnS particles on the film and then baked at 150 ℃ in the air environment to eliminate the moisture produced from aqueous solution.

3.3 Analytical Technologies

In this section, three analytical facilities will be presented, including SEM, EDX, and UV-VIS spectrometer. Numerical analysis used to estimate coverage properties of the film by MATLAB will be mentioned.

3.3.1 Scanning Electron Microscopy (SEM)

Scanning electron microscope (SEM) is a facility which can examine samples' topography and morphology. Unlike the conventional optical microscope, SEM utilizes electrons to reveal the image of the sample.

In SEM, there are two methods to generate electrons: thermionic and field-emission. The generated electrons by thermionic or field-emission methods are accelerated between a cathode and an anode and then the electrons are focused into a small-diameter electron probe. Electric or magnetic fields, applied at right angles, can be used to adjust the electrons direction for scanning the film surface. A schematic of SEM system is illustrated in Fig. 19. Since the pressure in the sample chamber usually amounts to about 10^{-4} Pa, the electron beam is allowed to travel from the cathode to the sample with little interaction with the residual gas molecules.

When the accelerated high-energy electron beam bombards the sample, the interaction between the electron beam and the sample generates a variety of responses, including secondary electrons emission, back scattered electrons emission, x-ray emission, and Auger electrons emission. By collecting and analyzing the resulted responses and signals, the image is formed on a monitor.

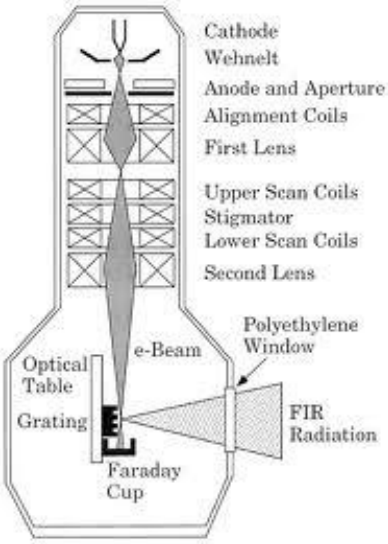

Fig. 19 Schematic of SEM system

Fig. 20 SEM in NCTU

3.3.2 Energy Dispersive X-ray Spectroscopy (EDX)

Energy dispersive X-ray spectroscopy (EDX) is capable for identifying heavy elements. The EDX technique is a specific technique used for the detection of the characteristic X-ray. The emission of the characteristic X-ray is produced by inner-shell excitation. The characteristic X-ray corresponds to each element because each element has specific energy in inner-shell.

The identification of element from the emission of the characteristic X-ray is as followed. After the generated characteristic X-ray transfers into a detector, the detector converts the incoming X-ray photons into electron-hole pairs. The electron-hole pairs are driven out of the detector and further converted to an electronic pulse by a charge-sensitive preamplifier. The amplitude of the pulse is proportional to the energy of the detected X-ray. A signal corresponding to the energy is processed into the appropriate channel of a multi-channel analyzer. The signal processing electronics calculates the number of pulses, resulting in a histogram of X-ray energy versus intensity.

Furthermore, because of the X-ray absorption in the beryllium detector window and in the lithium-drifted silicon chip, elements with atomic number less than ten are not identified usually.

3.3.3 UV-VIS Spectrometer

UV-VIS spectrometer is the instrument used to analyze the sample responses to different wavelengths of light, including reflection, transmittance, and absorption. When an electron in molecule is under the light irradiation, the electron will absorb the light energy. The specific light energy which results in electronic transitions in the ultraviolet (UV) and visible (VIS) range is named as the UV-VIS spectrum.

Qualitative measurement by UV-VIS spectrum can characterize the specific wavelength absorption of each functional group because the specificity of functional group. Molecular electronic binding orbitals are simply divided into three kinds; σ: single bond; π: double bond; n: not-binding electron pair. Several energy transitions are feasible such as σ→n, σ→σ*, n→π* and π→π* (as shown in Fig. 21). The energy required of n→π* and π→π* is fell in UV-VIS spectral range, so most applications are used in energy transitions n→π* and π→π*.

By measuring the difference of the initial incident light and the light interacted with the sample, the spectrum from ultraviolet to visible can be determined. Before the measurement in this UV-VIS spectrometer, the alto-zero process records the reflection, transmittance, or absorption of substrates, so the effects by substrates can be ignored during the analysis.

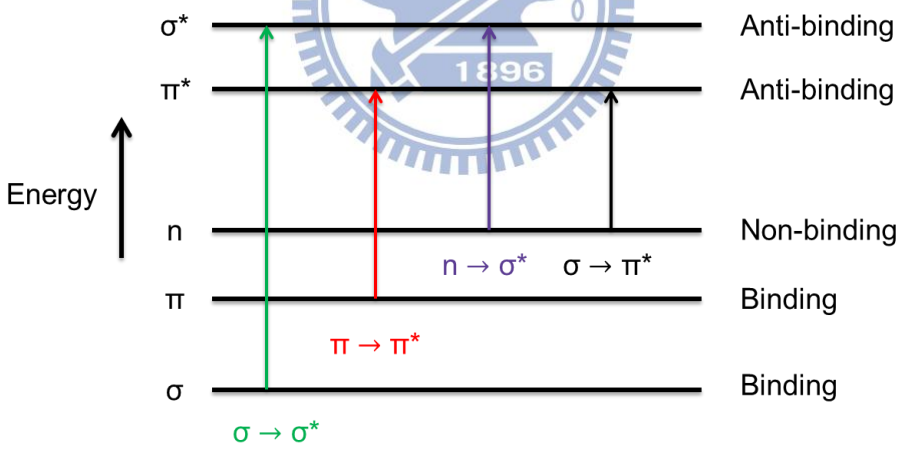

Fig. 21 Energy transitions between different binding orbitals

Fig. 22 UV-VIS Spectrometer in NCTU

3.3.4 MATLAB Coverage Analysis

In order to analyze the coverage properties of the ZnS surface morphology on the SLG in SEM results, numerical analysis by MATLAB are used. A schematic of a SEM result of ZnS surface morphology is shown in Fig. 23.

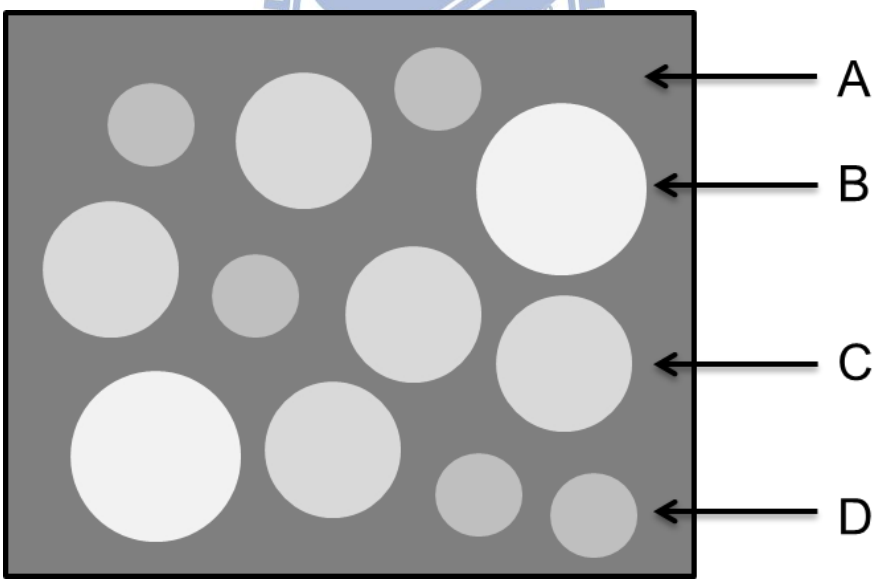

Fig. 23 A schematic of the SEM results of ZnS surface morphology

In Fig. 23, point A is located on the substrate. Point B, point C, and point D are related to different particle size with different gray level. First, the gray level of point A, point B, point C, and point D are defined as a', b', c', and d', respectively. In

general, the value of a’ is the smallest in the four number. Then, re-define the gray level, the values in the figure larger than a’ correspond to black and the values in the figure smaller than a’ correspond to white. The re-defined result is shown in Fig. 24.

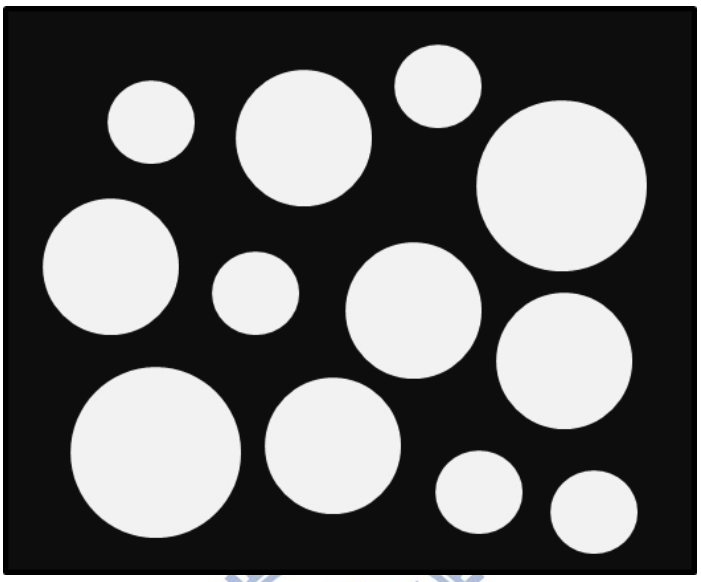

Fig. 24 A schematic after image processing

By calculating the area of white and the area of black, the area of white is obtained as W and the area of black is obtained as B. Finally, the film coverage properties W/ (W+B) can be obtained. It shall be noted that the film coverage properties by MATLAB numerical analysis is the estimation.

Chapter 4 Results and Discussion

4.1 Basic Characteristics

To achieve suitable stoichiometric ratio, well coverage, and thin-thickness ZnS film in chemical bath deposition, temperature, ammonia concentration, and deposition time of chemical bath solution were investigated on the ZnS film properties. Therefore, the influences of the temperature, the ammonia concentration, and the deposition time in solution were investigated to optimize the ZnS film properties.

4.1.1 Temperature

From experimental experience data, the solution temperature selected over 90 ℃ was unsuitable because the solution boiled dramatically and became unstable for film deposition. The boiling solution caused excessive reaction rate and undesirable perturbation and then resulted in the poor ZnS formation. Otherwise, the solution temperature below 60 ℃ was also unsuitable because of low reaction rate. Therefore, the temperature should be set between 65 and 85 ℃.

The ZnS deposition was performed with a solution consisting of 0.1 M $ZnSO_4$, 0.4 M $CS(NH_2)_2$, and 6 M ammonia in concentration. The solution temperatures were set to be 70 and 80 ℃ to determine the temperature effects on the depositing ZnS films. The deposition time was 50 minutes in both temperatures. The SEM results of both samples were shown in Fig. 25.

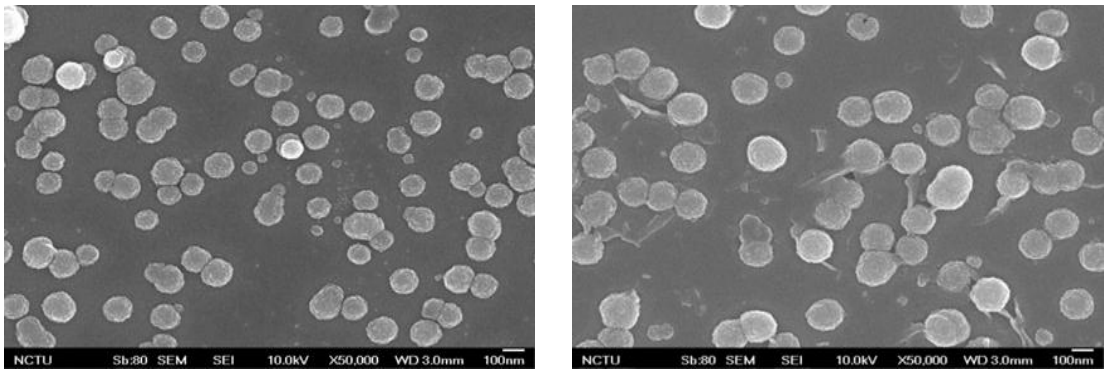

(a) **(b)**

Fig. 25 The SEM results of ZnS surface morphology deposited at (a) 70 ℃ and (b) 80 ℃

In Figs. 25 (a) and 25 (b), the sizes of the particles were about 100 nm and 120 nm, respectively. The larger particles could be observed in Fig. 25 (b) because the higher temperature provided more energy for particle growth and increased reaction rate. The EDX results of each sample were shown in Table 7. From the EDX results, the Zn/S ratio in the sample deposited at 80 ℃ was 2.54 and at 70 ℃ was 4.15, which meant there were more ZnS in the sample deposited at 80 ℃ than at 70 ℃. From database in LANGE'S HANDBOOK OF CHEMISTRY [29], the enthalpies of $Zn(OH)_2$ and ZnS were -641.91 and -192.6 KJ/mol, respectively. So the increasing proportion of ZnS was much larger than that of $Zn(OH)_2$ when temperature raised. Therefore, the particles acquiring more energy grew larger and ZnS were easier to form at higher temperature.

Table 7 The EDX results of ZnS deposited at (a) 70 ℃ and (b) 80 ℃

Sample	(a)		(b)	
Element	Weight (%)	Atomic (%)	Weight (%)	Atomic (%)
S	10.56	19.41	16.16	28.21
Zn	89.44	80.59	83.84	71.79
Zn/S	-	*4.15*	-	*2.54*

4.1.2 Ammonia Concentration

From experimental experience data, the ammonia concentration selected between 2 M and 6 M was appropriate. Ammonia concentration over 6 M was unsuitable because it would decrease the solution's boiling point and then caused the solution boiling easily. Ammonia concentration below 2 M was too low to form complex ions which were helpful for controlling the concentration of Zn^{2+} and reaction rate in the solution.

The ZnS deposition was performed with a solution consisting of 0.1 M $ZnSO_4$, 0.4 M $CS(NH_2)_2$ in concentration. 2 M and 4 M ammonia concentration were compared to determine the ammonia concentration effects on the ZnS films. The solution temperature was set to be 80 ℃ and the substrates were deposited in the solution for 50 minutes. The SEM results of both samples were shown in Fig. 26.

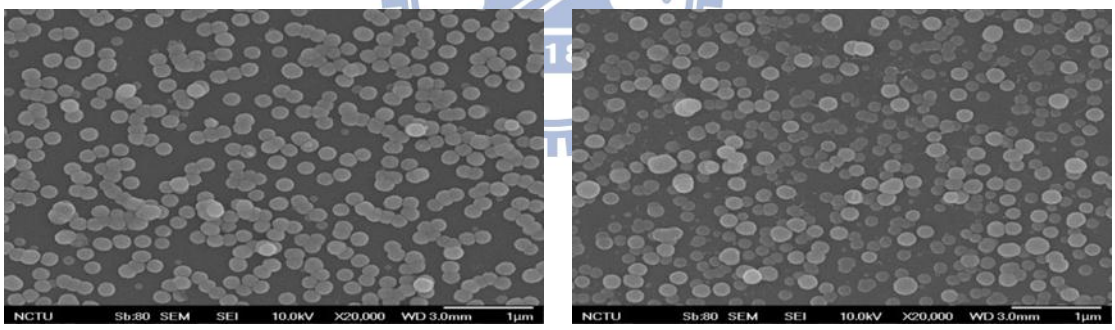

(a) **(b)**

Fig. 26 The SEM results of ZnS surface morphology deposited at (a) 2 M and (b) 4 M in ammonia mole concentration

It was reported that the formation of $Zn(OH)_2$ was cluster nucleation [30]. Particles formed in cluster nucleation was easier to cluster and became larger, so the $Zn(OH)_2$ particles were larger than ZnS particles. Higher ammonia concentration provided more OH^- which easily caused the $Zn(OH)_2$ formation as shown in reaction Table 6 (5). Therefore, the observed large particles in Fig. 26 (b) mainly were

assumed to be $Zn(OH)_2$ particles.

The EDX results of each sample were shown in Table 8. From the EDX results, the Zn/S ratio in 2 M and 4 M ammonia concentrations were 2.03 and 2.34, respectively. The Zn/S ratio in 2 M ammonia concentrations was less than the Zn/S ratio in 4 M ammonia concentrations, which also indicated that there were more $Zn(OH)_2$ forming in the sample deposited in 4 M ammonia concentrations.

The particles' sizes observed in Fig. 26 (a) were more uniform than those in Fig. 26 (b), because sample growing in higher ammonia concentration would form more $Zn(OH)_2$ particles. Therefore, the sample growing in lower ammonia concentration was preferred.

Table 8 The EDX results of ZnS deposited at (a) 2 M and (b) 4 M in ammonia mole concentration

Sample	(a)		(b)	
Element	Weight (%)	Atomic (%)	Weight (%)	Atomic (%)
S	19.44	32.97	17.3	29.9
Zn	80.56	67.03	82.7	70.1
Zn/S	-	*2.03*	-	*2.34*

4.1.3 Deposition Time

The ZnS deposition was performed with a solution consisting of 0.1 M $ZnSO_4$, 0.4 M $CS(NH_2)_2$, and 3 M ammonia in concentration. The temperature was set to be 85 ℃ and the deposition times were selected from 10 to 50 minutes. The SEM results and EDX results of five samples are shown in Fig. 27 and Table 9, respectively.

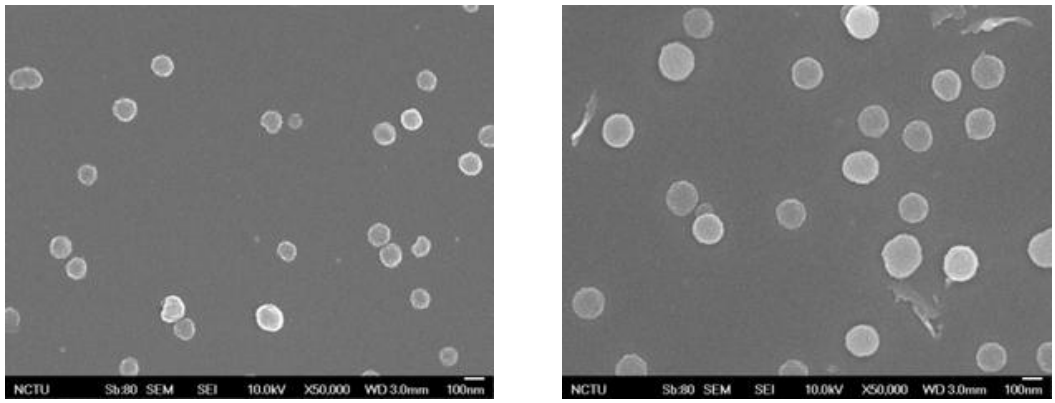

(a) **(b)**

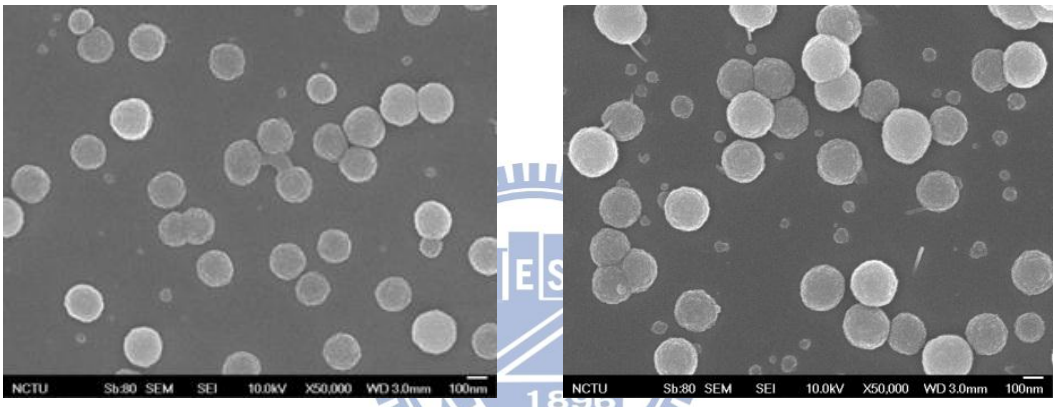

(c) **(d)**

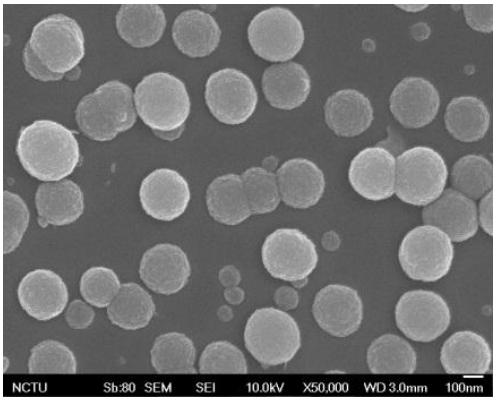

(e)

Fig. 27 The SEM results of ZnS surface morphology deposited for (a) 10 minutes, (b) 20 minutes, (c) 30 minutes, (d) 40 minutes, and (e) 50 minutes

Table 9 The EDX results of ZnS deposited for (a) 10 minutes, (b) 20 minutes, (c) 30 minutes, (d) 40 minutes, and (e) 50 minutes

Sample	Element	S	Zn	Zn/S
(a)	Weight (%)	6.43	93.57	-
	Atomic (%)	12.28	87.72	*7.14*
(b)	Weight (%)	8.54	91.46	-
	Atomic (%)	15.99	84.01	*5.25*
(c)	Weight (%)	11.05	88.95	-
	Atomic (%)	20.21	79.79	*3.95*
(d)	Weight (%)	14.69	85.31	-
	Atomic (%)	25.99	74.01	*2.85*
(e)	Weight (%)	17.79	82.21	-
	Atomic (%)	30.60	69.40	*2.27*

From the EDX results, the particles deposited on SLG mainly were $Zn(OH)_2$ particles in the first 30 minutes. With the increasing deposition time, the continuous of zinc hydroxide deposition and sulfide substitution formed the ZnS particles. The Zn/S ratio reached 2.27 after depositing for 50 minutes. The sizes of particles deposited in 10, 20, 30, 40, and 50 minutes were about 78, 95, 118, 149, and 186 nm, respectively.

The relationship between deposition time and the thickness was shown in Fig. 28, and the relationship between deposition time and the Zn/S ratio was shown in Fig. 29. The sizes of particles were linearly related to deposition time, yet the particles over 150 nm were not suitable to grow on CIGS absorber. From Fig. 29, the trend of Zn/S ratio curve approached flat when the sample deposited for 50 minutes, which indicated the substitution was nearly saturated about 50 minutes and the Zn/S ratio was hard to decrease. To sum up, the film properties deposited in the one-step deposition were not good enough at stoichiometric ratio and coverage properties.

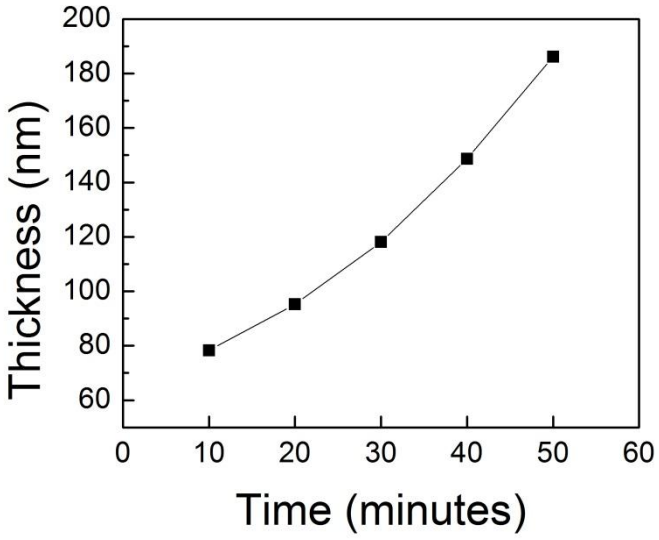

Fig. 28 The relationship between deposition time and the thickness of five ZnS films

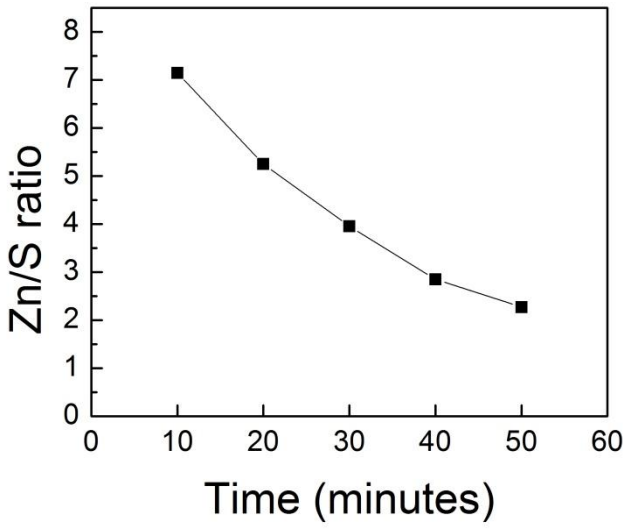

Fig. 29 The relationship between deposition time and the Zn/S ratio of five ZnS films

4.1.4 Summary

At higher temperature, the particles acquiring more energy grew larger and the ZnS particles formed easily. The samples growing in higher ammonia concentration would contain more $Zn(OH)_2$ particles and caused non-uniform films growth. The samples were mainly formed by $Zn(OH)_2$ particles in about the first 30 minutes then the OH^- were substituted by S^{2-} to form ZnS with the increase of deposition time. From the results, the films deposited by one-step deposition were not good enough at stoichiometric ratio and coverage properties.

4.2 Deposition Improvements

During the chemical bath deposition, film properties were not good enough in one-step deposition, so post-deposition and two-step deposition were proposed to improve the film properties.

4.2.1 Post-deposition

The post-deposition was a post-treatment used to improve the film properties after the deposition. Because the $Zn(OH)_2$ particles could dissolve and become activated in ammonia solution [36] as well as OH^- could be substituted by S^{2-} as shown in Table 6, the as-deposited films were post-deposited in ammonia solution and thiourea solution for further improvements. To show the effects by post-deposition, the samples with and without post-deposition were compared. The ZnS deposition was performed with a solution consisting of 0.1 M $ZnSO_4$, 0.4 M $CS(NH_2)_2$, and 3 M ammonia in concentration to determine the post-deposition improvements on ZnS film properties. The solution temperature and the deposition time were set to be 85 ℃ and 30 minutes, respectively. After the first-step deposition, the films were

post-deposited under ammonia solution and 0.4 M $CS(NH_2)_2$ solution, respectively. The SEM result of the film without post-deposited was shown in Fig. 30 (a). The SEM results of the films with post-deposited under ammonia solution and 0.4M $CS(NH_2)_2$ solution were shown in Figs. 30 (b) and 30 (c), respectively. The EDX results of all ZnS films were shown in Table 10.

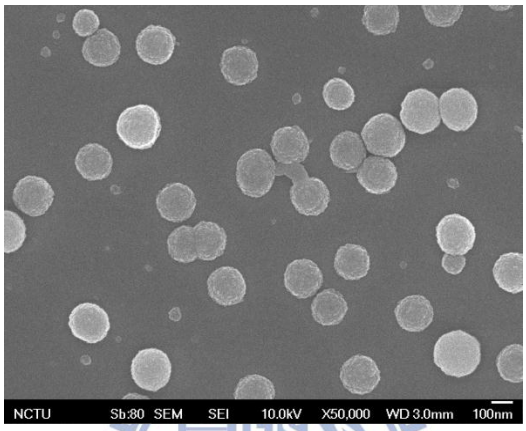

(a)

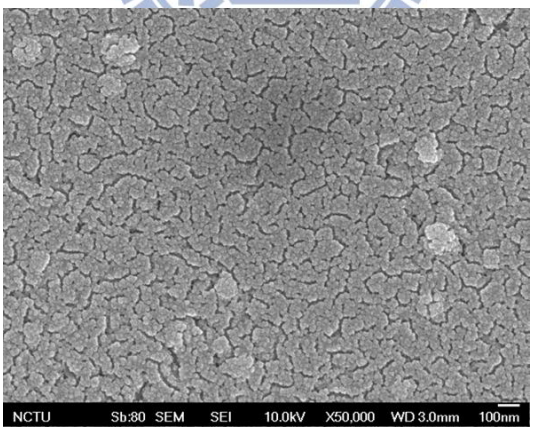

(b)

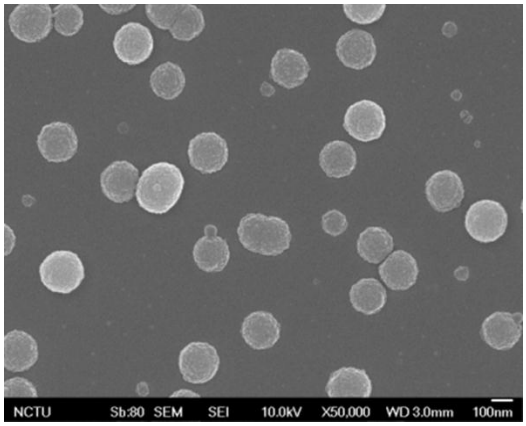

(c)

Fig. 30 The SEM results of ZnS surface morphology (a) without post-deposition, (b) under ammonia post-deposition, and (c) under thiourea post-deposition

Table 10 The EDX results of ZnS (a) without post-deposition, (b) ammonia post-deposition (c) thiourea post-deposition

Sample	(a) without post-deposition		(b) ammonia post-deposition		(c) thiourea post-deposition	
Element	Weight (%)	Atomic (%)	Weight (%)	Atomic (%)	Weight (%)	Atomic (%)
S	11.05	20.21	13.81	24.61	15.17	26.71
Zn	88.95	79.79	86.19	75.39	84.83	73.29
Zn/S	-	*3.95*	-	*3.06*	-	*2.74*

The results showed that the sample deposited under ammonia solution was activated by ammonia so surface morphology of the film reformed and the film coverage properties were improved. The surface morphology of sample deposited under thiourea solution was not changed significantly. Besides, the Zn/S ratios were decreased from 3.95 in the first-deposition to 3.06 under ammonia solution and 2.74 under thiourea solution. Therefore, by continuously modifying and combining the ammonia post-deposition and the thiourea post-deposition, the results were further

improved.

The modified solution condition was the same in the first-step deposition. The films after the first-step deposition were post-deposited under the solution consisted of 0.4 M $CS(NH_2)_2$ and 10 M ammonia in concentration. In the post-deposition, the temperature was set to be 50 ℃ to provide energy for films growth and the post-deposition time were 10 and 20 minutes, respectively. The SEM result of ZnS surface morphology without post-deposition was shown in Fig. 31 (a). The SEM results of ZnS surface morphology with post-deposition for 10 and 20 minutes were shown in Figs. 31 (b) and 31 (c), respectively. The EDX results were shown in Table 11.

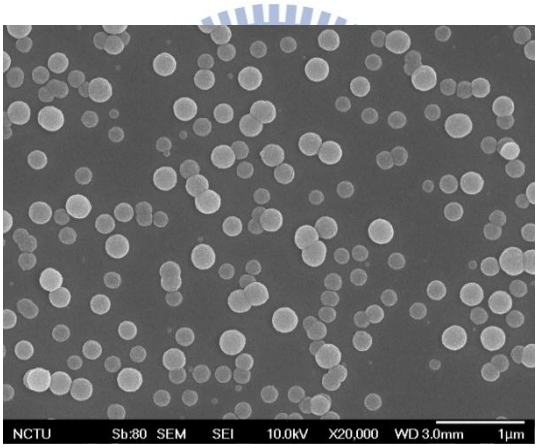

(a)

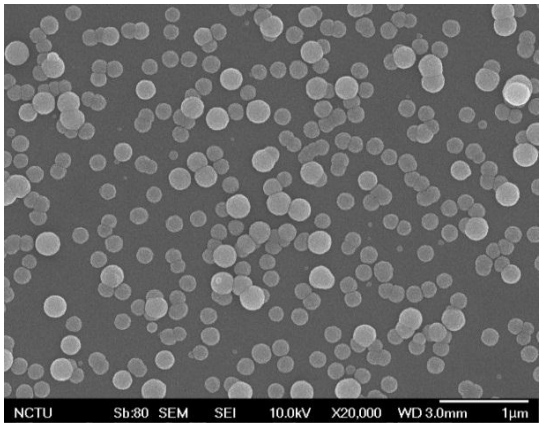

(b)

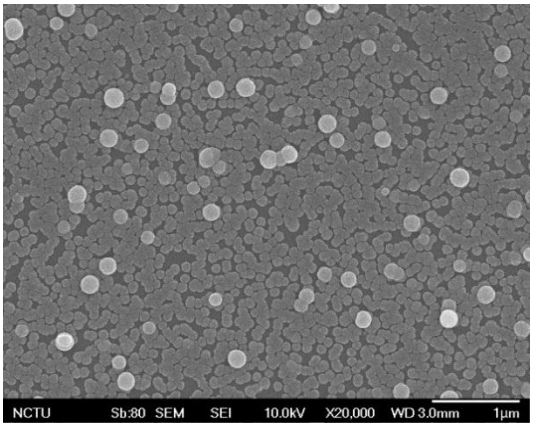

(c)

Fig. 31 The SEM results of ZnS surface morphology (a) without post-deposition, (b) post-deposited for 10 minutes, and (c) post-deposited for 20 minutes

Table 11 The EDX results of ZnS (a) without post-deposition, (b) post-deposition for 10 minutes, and (c) post-deposition for 20 minutes

Sample	(a) without post-deposition		(b) post-deposition for 10 minutes		(c) post-deposition for 20 minutes	
Element	Weight (%)	Atomic (%)	Weight (%)	Atomic (%)	Weight (%)	Atomic (%)
S	11.28	20.58	13.85	24.68	16.56	28.80
Zn	88.72	79.42	86.15	75.32	83.44	71.20
Zn/S	-	*3.86*	-	*3.05*	-	*2.47*

From the EDX results, the Zn/S ratios were 3.95, 3.05, and 2.47 in three different steps. By combining both post-deposition advantages, the Zn/S ratio was decreased from 3.95 in the first-deposition to 2.47 after the post-deposition and the film achieved high coverage. The thickness of the ZnS film post-deposited for 20 minutes was about 146 nm. Therefore, post-deposition in the thiourea and ammonia solution decreased the Zn/S ratio and improved coverage properties of ZnS films, but the stoichiometric ratio and the thickness were not good enough.

4.2.2 Two-step Deposition

Two-step deposition was then proposed to improve the film properties. From the cluster mechanism discussed in section 2.3.4, the films were formed by $Zn(OH)_2$ nucleation, then ZnS films are easier to form with the help of $Zn(OH)_2$ nucleation. Based on this mechanism, two-step deposition included two steps: nucleation and film formation. By $Zn(OH)_2$ forming in first-step deposition and ZnS film forming in second-step deposition, the films could achieve high-coverage and desirable stoichiometric ratio.

A series experiments were conducted to evaluate the two-step deposition. In the series experiments, all of the solutions consisted of 0.1 M $ZnSO_4$, 0.4 M $CS(NH_2)_2$, and 3 M ammonia in concentration. From the basic characteristics, it was found that the films formed around the first 30 minutes mainly were $Zn(OH)_2$. Consequently, the temperature was set to be 85 °C in the first-step deposition ranged from 20 to 40 minutes to form $Zn(OH)_2$ and 70 °C in the second-step deposition ranged from 10 to 30 minutes for ZnS film forming. The films deposited for 20 minutes in first-step and further deposited for 10, 20, and 30 minutes in second-step were shown in Figs. 32 (a), 32 (b), 32 (c), and 32 (d), respectively. The films deposited for 30 minutes in first-step and further deposited for 10, 20, and 30 minutes in second-step were shown in Figs. 33 (a), 33 (b), 33 (c), and 33 (d), respectively. The films deposited for 40 minutes in first-step and further deposited for 10, 20, and 30 minutes in second-step were shown in Figs. 34 (a), 34 (b), 34 (c), and 34 (d), respectively. The SEM cross-section results of ZnS surface morphology of 32 (d), 33 (d), and 34 (d) films were shown in Figs. 35. The EDX results of the three series experiments were shown in Tables 12, 13, and 14, respectively. Between the first-step and second-step deposition, the films were treated

with ultrasonic cleaning at 50 ℃ to remove loose particles formed in the first-step deposition and maintain the film activation after the first-step deposition.

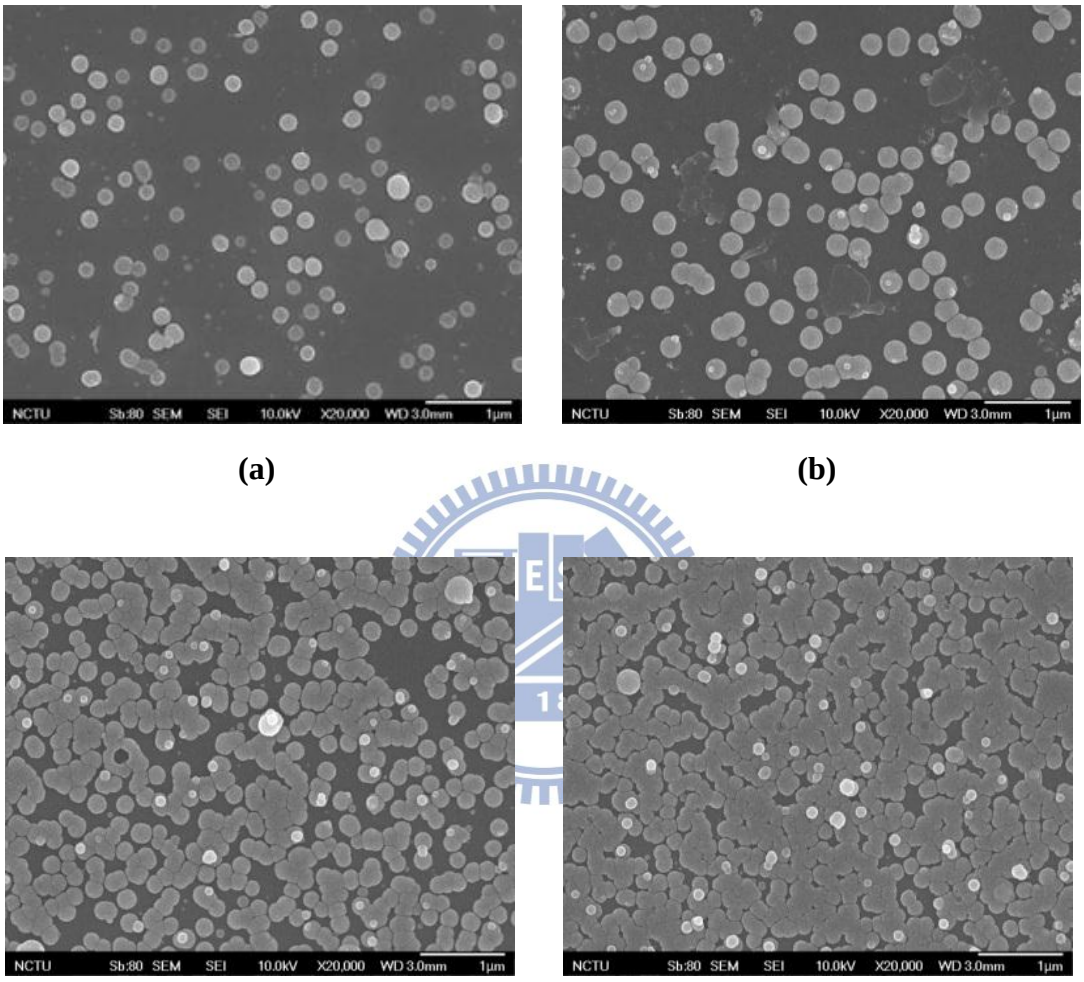

Fig. 32 The SEM results of ZnS surface morphology deposited for 20 minutes in first-step deposition (a) without further deposition, (b) further deposited for 10 minutes, (c) further deposited for 20 minutes, and (d) further deposited for 30 minutes

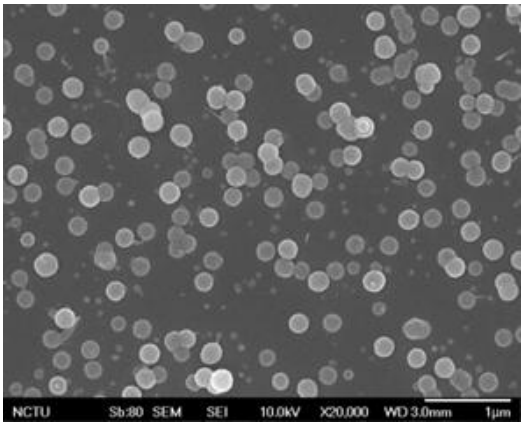

(a)

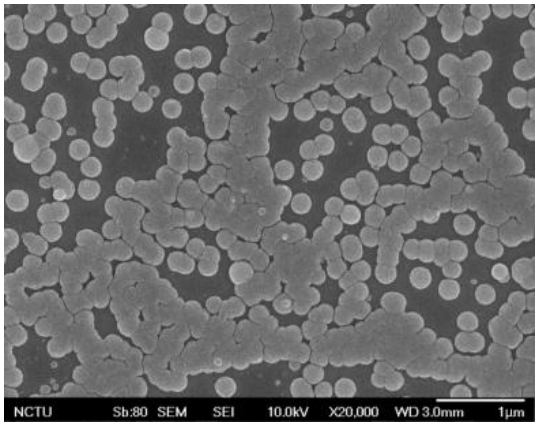

(b)

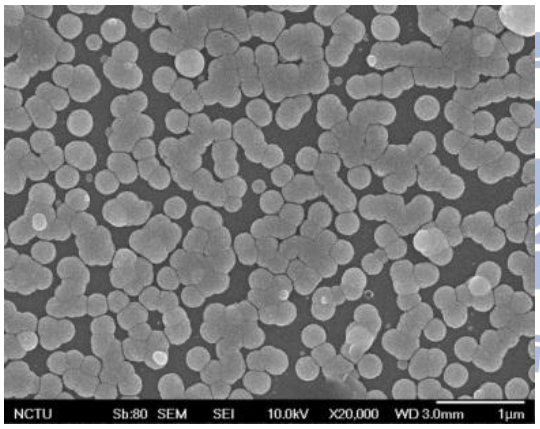

(c)

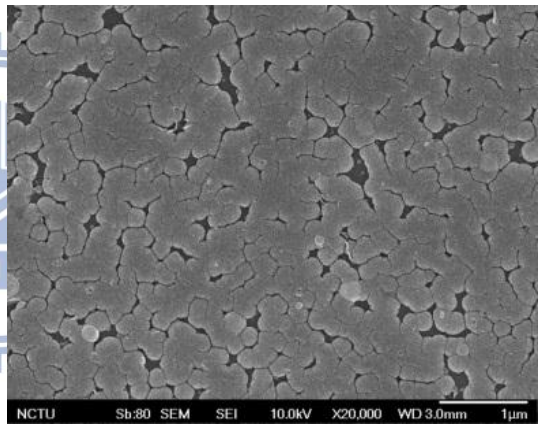

(d)

Fig. 33 The SEM results of ZnS surface morphology deposited for 30 minutes in first-step deposition (a) without further deposition, (b) further deposited for 10 minutes, (c) further deposited for 20 minutes, and (d) further deposited for 30 minutes

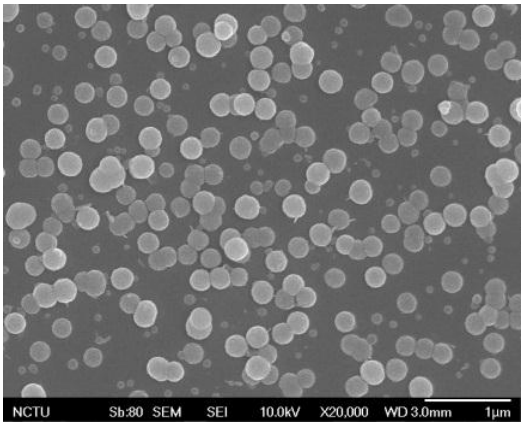

(a)

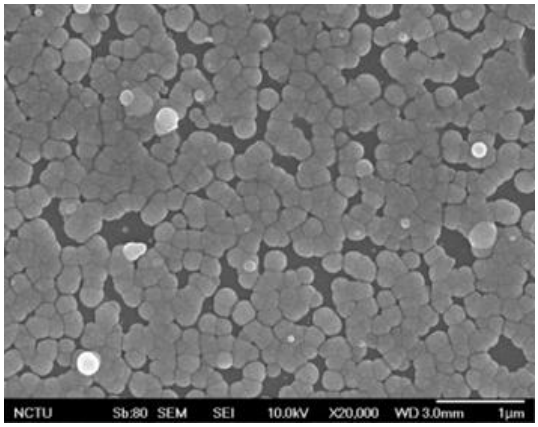

(b)

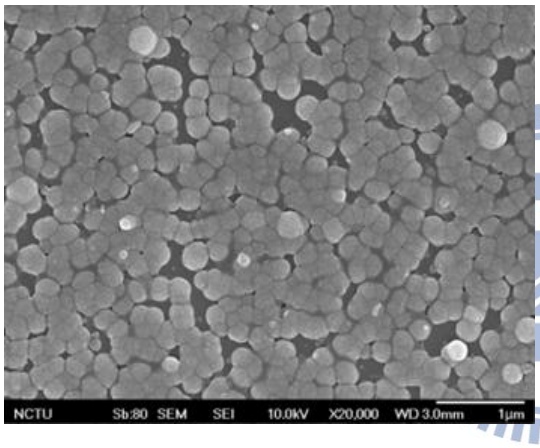

(c)

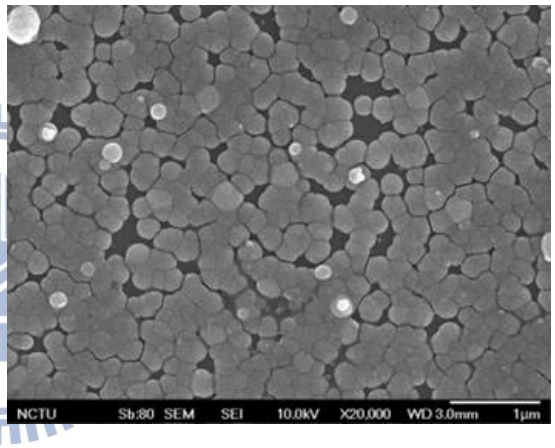

(d)

Fig. 34 The SEM results of ZnS surface morphology deposited for 40 minutes in first-step deposition (a) without further deposition, (b) further deposited for 10 minutes, (c) further deposited for 20 minutes, and (d) further deposited for 30 minutes

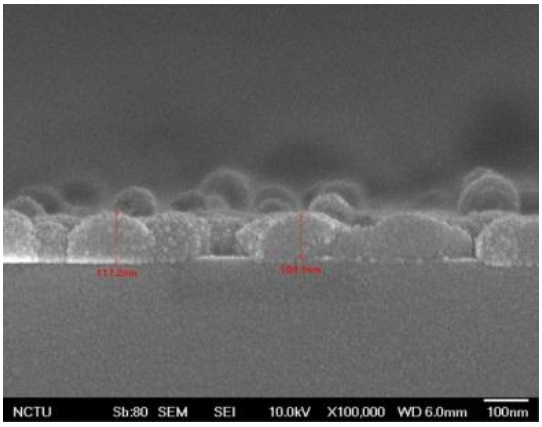

(a)

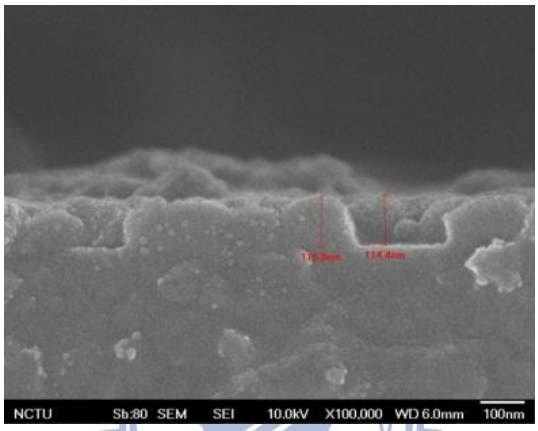

(b)

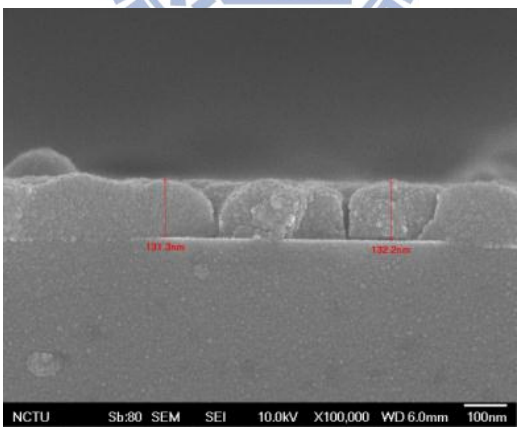

(c)

Fig. 35 The SEM cross-section results of ZnS surface morphology of (a) Fig. 32-(d), (b) Fig. 33-(d), and (c) Fig. 34-(d)

Table 12 The EDX results of ZnS deposited for 20 minutes in first-step deposition, and then (a) without further deposition, (b) further deposited for 10 minutes, (c) further deposited for 20 minutes, and (d) further deposited for 30 minutes

Sample	(a)		(b)	
Element	Weight (%)	Atomic (%)	Weight (%)	Atomic (%)
S	8.71	16.28	13.39	23.96
Zn	91.29	83.72	86.61	76.04
Zn/S	-	*5.14*	-	*3.17*
Sample	(c)		(d)	
Element	Weight (%)	Atomic (%)	Weight (%)	Atomic (%)
S	18.06	31.00	20.31	34.19
Zn	81.94	69.00	79.69	65.81
Zn/S	-	*2.23*	-	*1.92*

Table 13 The EDX results of ZnS deposited for 30 minutes in first-step deposition, and then (a) without further deposition, (b) further deposited for 10 minutes, (c) further deposited for 20 minutes, and (d) further deposited for 30 minutes

Sample	(a)		(b)	
Element	Weight (%)	Atomic (%)	Element	Weight (%)
S	11.15	20.36	19.58	33.17
Zn	88.85	79.64	80.42	66.83
Zn/S	-	*3.91*	-	*2.01*
Sample	(c)		(d)	
Element	Weight (%)	Atomic (%)	Element	Weight (%)
S	22.07	36.60	22.16	36.72
Zn	77.93	63.40	77.84	63.28
Zn/S	-	*1.73*	-	*1.72*

Table 14 The EDX results of ZnS deposited for 40 minutes in first-step deposition, and then (a) without further deposition, (b) further deposited for 10 minutes, (c) further deposited for 20 minutes, and (d) further deposited for 30 minutes

Sample	(a)		(b)	
Element	Weight (%)	Atomic (%)	Element	Weight (%)
S	14.69	25.99	20.25	34.10
Zn	85.31	74.01	79.75	65.90
Zn/S	-	*3.03*	-	*1.93*
Sample	(c)		(d)	
Element	Weight (%)	Atomic (%)	Element	Weight (%)
S	20.89	34.99	21.43	35.73
Zn	79.11	65.01	78.57	64.27
Zn/S	-	*1.86*	-	*1.80*

For simplicity, the films deposited for 20 minutes in the first-step and further deposited for 10, 20, and 30 minutes in the second-step will be described as (20, 0), (20, 10), (20, 20), and (20, 30), respectively. Also the same description as (30, 0), (30, 10), (30, 20), and (30, 30) are the films deposited for 30 minutes in the first-step and further deposited for 10, 20, and 30 minutes. (40, 0), (40, 10), (40, 20), and (40, 30) are the films deposited for 40 minutes in the first-step and further deposited for 10, 20, and 30 minutes.

From the SEM results, all the films further deposited for 30 minutes, which were the (20, 30), (30, 30), and (40, 30) films, were found to achieve high coverage on SLG. To show the coverage properties, the MATLAB Numerical Analysis was used in each film. The coverage estimation of (20, 0), (20, 10), (20, 20), and (20, 30) films were 18.70 %, 35.67 %, 67.07 %, and 82.14 %, respectively. The coverage estimation of (30, 0), (30, 10), (30, 20), and (30, 30) films were 29.87 %, 63.67 %, 73.52 %, and 94.59 %, respectively. The coverage estimation of (40, 0), (40, 10), (40, 20), and (40,

30) films were 36.65 %, 78.11 %, 82.22 %, and 88.51 %, respectively. The relationship between deposition time and the coverage properties of each deposition condition were shown in Fig. 36.

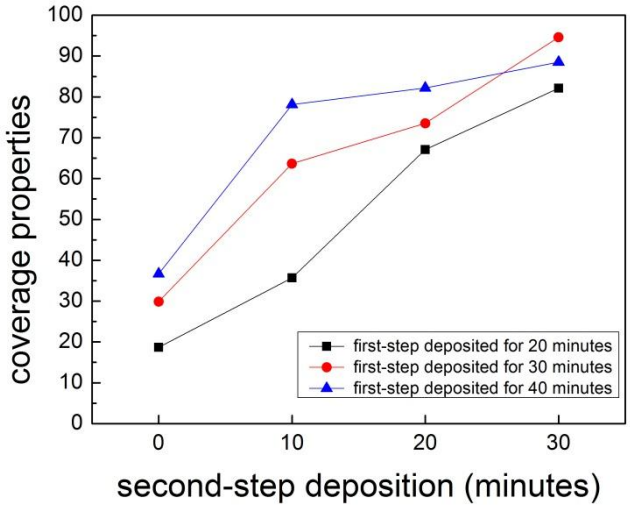

Fig. 36 The relationship between deposition time and the coverage properties of each deposition condition

From Fig. 36, for (20, 30), (30, 30), and (40, 30) film, the coverage properties reached 82.14 %, 94.59 %, and 88.51 %, so (20, 30), (30, 30), and (40, 30) films can achieve over 80 % coverage properties on SLG. The (40, 30) film only reached 88.51 % coverage properties which was not better than the coverage properties of (30, 30) film. It is believed that the $Zn(OH)_2$ particles grown in the first-step deposition were too large in (40, 0) film, so the large $Zn(OH)_2$ particles caused ZnS film formed in the second-step deposition were hard to form a continuous surface and cover the surface of substrates. In three different deposition conditions, the (30, 30) film reached 94.59 % coverage properties, the highest coverage film in the three films.

From the EDX results, the Zn/S ratio of (20, 0), (20, 10), (20, 20), and (20, 30)

films were 5.25, 3.17, 2.23, and 1.92, respectively. The Zn/S ratio of (30, 0), (30, 10), (30, 20), and (30, 30) films were 3.95, 2.01, 1.73, and 1.72, respectively. The Zn/S ratio of (40, 0), (40, 10), (40, 20), and (40, 30) films were 3.03, 1.93, 1.86, and 1.80, respectively. The relationship between the Zn/S ratio and second-step deposition of each film is shown in Fig. 37.

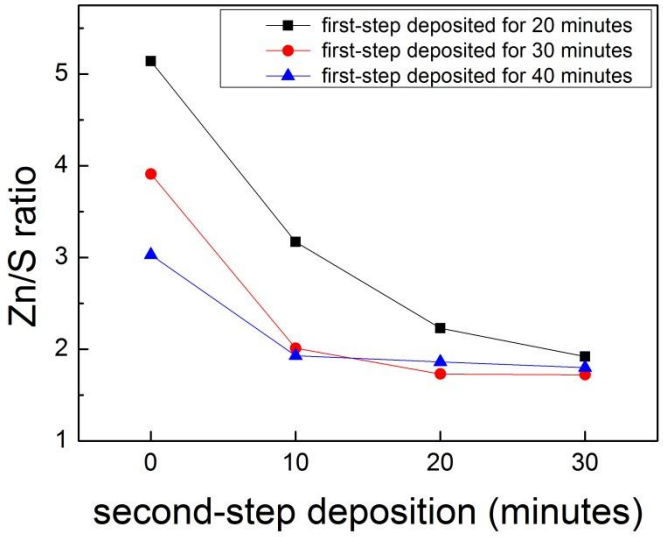

Fig. 37 The relationship between the Zn/S ratio and second-step deposition of each film

From Fig. 37, most of particles were $Zn(OH)_2$ in first-step deposition, and the Zn/S ratio of (20, 30), (30, 30), and (40, 30) films reached around 1.8 after second-step deposition. For the (40, 10), (40, 20), and (40, 30) films, the Zn/S ratios were 1.93, 1.86, and 1.80, respectively. For (30, 20) and (30, 30) films, the Zn/S ratios were 1.73 and 1.72. The Zn/S ratios from (40, 10) film to (40, 30) film varied slightly. Also the Zn/S ratios from (30, 20) film to (30, 30) film varied slightly again. The slightly-vary Zn/S ratios indicated the S^{2-} substitution reactions were almost in equilibrium when total deposition time reached around 50 minutes. Therefore, to achieve desired Zn/S ratios, the deposition condition must be selected carefully.

The transmittances of the (20, 30), (30, 30), and (40, 30) films measured by UV-VIS Spectrometer were shown in Fig. 38. The thickness of the (20, 30), (30, 30), and (40, 30) films were about 110, 116, and 130 nm, respectively.

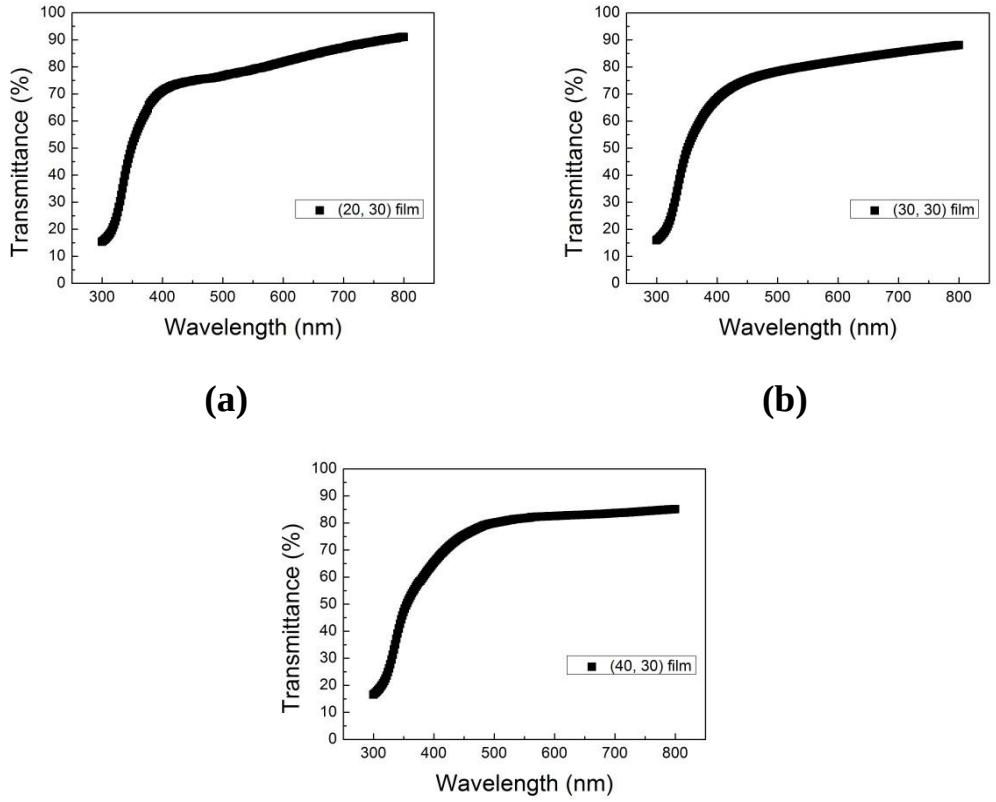

(a) **(b)**

(c)

Fig. 38 The transmittance of (a) (20, 30) film, (b) (30, 30) film, and (c) (40, 30) film

To identify the transmittances of ZnS films, the average transmittances from 300 nm to 800 nm were used. The average transmittances of the (20, 30), (30, 30), and (40, 30) films were about 74.60 %, 73.88 %, and 73.17 %, respectively. It is known that the thinner film achieved higher transmittance, yet the transmittances of ZnS films affected by the thickness were inappreciable. For general cases, the average transmittances of ZnS films over 70% were suitable. Therefore, for the transmittances,

the three ZnS films were acceptable.

The band-gap of (20, 30), (30, 30), and (40, 30) films were measured from the transmittances results as shown in Fig. 38. The band-gap of (20, 30), (30, 30), and (40, 30) films were about 3.60, 3.57 and 3.58, respectively.

The electrical characteristic of (30, 30) films which had the best properties in our results were measured. The (30, 30) films had electrical resistivity of 1.06×10^{1} Ω-cm and mobility of $1.19 \times 10^{5}\ cm/sV$. So the electrical characteristic of our films were acceptable.

4.2.3 Summary

The post-deposition and two-step deposition were investigated to improve films properties, including coverage properties, stoichiometric ratio, and thickness. By comparing two deposition methods, two-step deposition was found to achieve better performance such as high-coverage properties, suitable stoichiometric ratio, and thin-thickness than post-deposition. In two-step deposition, the film deposited for 30 minutes in first-step and further deposited for 30 minutes in second-step achieved 94.59 % coverage properties, 1.72 Zn/S stoichiometric ratios, and about 116 nm film thicknesses. Therefore, the ZnS films deposited by two-step deposition for 30 minutes in first-step and further deposited for 30 minutes were preferred to deposit on CIGS/Mo/SLG substrates.

4.3 ZnS Deposited on CIGS

To evaluate the practicality of two-step deposition, the ZnS films were deposited on CIGS/Mo/SLG substrates by two-step deposition. As mentioned in section 4.2.3, the ZnS films deposited by two-step deposition for 30 minutes in first-step and further deposited for 30 minutes achieved 94.59 % coverage properties, 1.72 Zn/S

stoichiometric ratios, and about 116 nm film thicknesses on SLG. Consequently, this two-step deposition condition was used to fabricate ZnS buffer layer on CIGS absorber layer. The SEM top-view and cross-section results of the ZnS films fabricated on CIGS/Mo/SLG substrates were shown in Figs. 38 and 39, respectively.

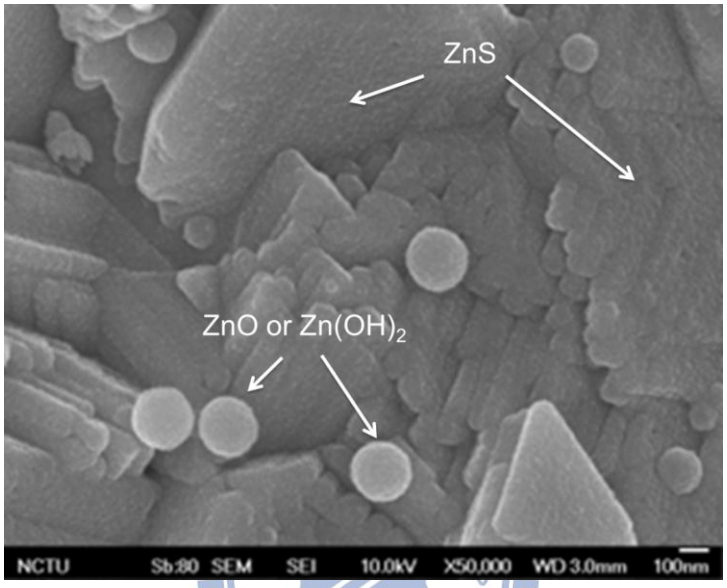

Fig. 39 The SEM top-view result of the ZnS surface morphology deposited on CIGS/Mo/SLG substrate

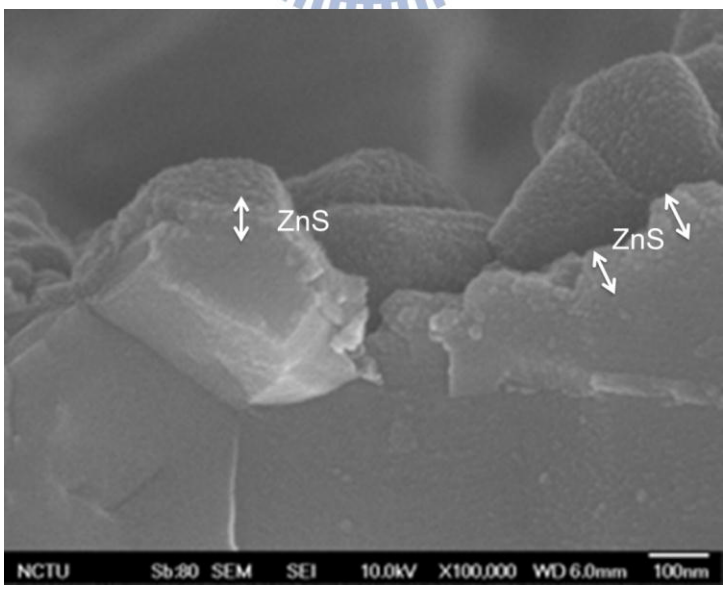

Fig. 40 The SEM cross-section result of the ZnS surface morphology deposited on CIGS/Mo/SLG substrate

From the SEM top-view result shown in Fig. 38, the ZnS film fully cover the surface of CIGS absorber layer. Although there were some ZnO or $Zn(OH)_2$ particles on the CIGS absorber layer, the ZnO particles did not occupy large areas. From SEM cross-section result, the ZnS film deposited on CIGS/Mo/SLG substrate was about 100 nm, which was suitable thickness as buffer layer for CIGS solar cells. From the EDX result, the Zn/S ratio of the ZnS film deposited on CIGS/Mo/SLG substrate was about 1.78, which was similar to the Zn/S ratio 1.72 grown on SLG. Therefore, the ZnS film deposited on CIGS/Mo/SLG substrate achieved over 95 % coverage properties, 1.78 Zn/S stoichiometric ratios, and about 100 nm film thicknesses. From the ZnS results fabricated by Nakada group [31], the ZnS film achieved 1.72 Zn/S stoichiometric ratios and about 100 nm film thicknesses on CIGS absorber layer. So the ZnS films deposited by two-step deposition in this thesis can achieve similar performance on CIGS absorber layer compared with ZnS films deposited by Nakada group.

Chapter 5 Conclusions and Future works

5.1 Conclusions

In chemical bath deposition methods, the ZnS films properties affected by the temperature and the ammonia concentration in chemical bath solution have been discussed. During the chemical bath deposition, the deposition time and the growth mechanism have been investigated to analyze the stoichiometric ratio, the coverage properties, and the thickness in different deposition time. From the results by one-step deposition, the ZnS films can not simultaneously reach suitable stoichiometric ratio, well coverage properties, and desired thin thickness. Therefore, two methods, post-deposition and two-step deposition, are proposed to further improve the films properties.

In the post-deposition, films deposited at 85 ℃ in one-step deposition for 30 minutes and at 50 ℃ in post-deposition for 20 minutes in 0.4 M $CS(NH_2)_2$ and 10 M ammonia solution achieved over 95 % coverage properties, 2.47 Zn/S stoichiometric ratios, and about 146 nm on SLG. So in post-deposition, the well coverage properties were achieved, but the suitable stoichiometric ratio and the thin thickness were not reached.

In the two-step deposition, the different conditions have been investigated to find out the suitable stoichiometric ratio, the well coverage properties, and the desired thin thickness. Films deposited at 85 ℃ in first-step for 30 minutes and at 70 ℃ in second-step for 30 minutes achieve 1.72 Zn/S stoichiometric ratios, about 95 % coverage properties, and about 100 nm thin-films on SLG, which are adopted to form ZnS film on CIGS/Mo/SLG substrate.

The comparison of two methods concluded that the two-step deposition is preferred to form ZnS films on CIGS absorber layer than post-deposition. The ZnS films deposited at 85 ℃ in first-step for 30 minutes and at 70 ℃ in second-step for 30 minutes are used to fabricate the ZnS buffer layer and achieve 1.78 Zn/S stoichiometric ratios, over 95 % coverage properties, and about 100 nm film thicknesses on CIGS/Mo/SLG substrate. On the other words, the modified two-step deposition is a suitable method to deposit the ZnS buffer layer in CIGS solar cells.

5.2 Future Works

ZnS films grown by two-step deposition achieve 1.78 Zn/S stoichiometric ratios, over 95 % coverage properties, and about 100 nm film thicknesses on CIGS absorber layer. To further improve the efficiency in CIGS devices fabricated with the ZnS buffer layer, the band-gap modulation is needed [32]. Due to a slight large conduction band offset between the CBD-ZnS and CIGS interface, carries are not easy to transfer when the carries arrive between the ZnS/CIGS interface. The band-gap modulation of V-shaped Ga distribution in CIGS absorber layer is a method which can help the carries transfer [33]. The band diagrams without band-gap modulation and with band-gap modulation are shown in Fig. 40.

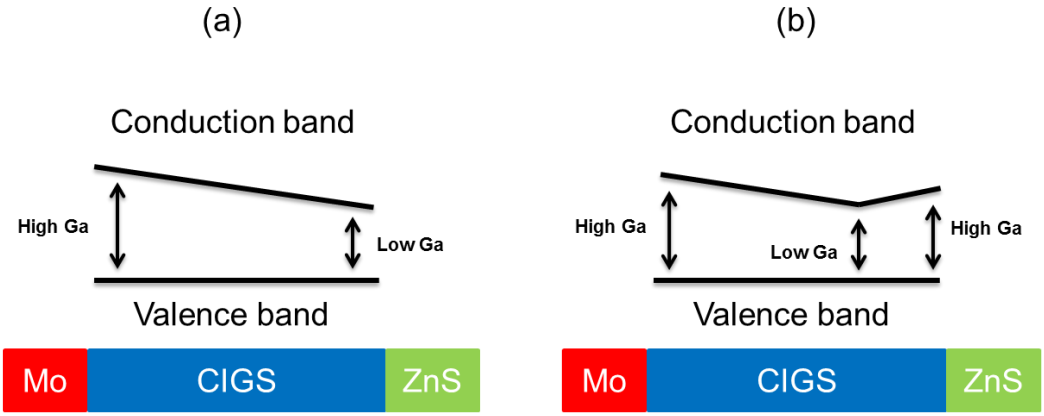

Fig. 41 The band diagram of (a) without band-gap modulation and (b) with band-gap modulation

However, the band-gap modulation of V-shaped Ga distribution in CIGS absorber layer is successfully realized by the CIGS co-evaporation process but is not accomplished in the selenization process of CIG precursors. Therefore, two methods, CIGS sulfurization [34] and gradient buffer layer [35], are proposed to improve the band-gap issues in the selenization process of CIG precursors.

CIGS sulfurization method is an evaporation process which is similar to the selenization process. The CIGS absorber layer after the sulfurization will form as $Cu(In,Ga)(S,Se)_2$ (CIGSS). Due to the participation of CIGS sulfurization process, the band-gap between the CIGSS absorber layer and the ZnS buffer layer is modulated, which is helpful for carries transferring and can improve the band offset issues.

The gradient buffer layer can be achieved by adding a buffer material between the CIGS absorber layer and ZnS buffer layer. The band-gap of this adding buffer material must be selected between the band-gap of CIGS and the band-gap of ZnS to form the gradient band-gap. Zinc selenide (ZnSe) is a material which satisfies the gradient band-gap condition. With the participation of ZnSe between the CIGS absorber layer and ZnS buffer layer, the band offset issues can be improved.

References

[1] J. Zhao, A. Wang, M. Green, and F. Ferrazza, *Applied Physics Letters*. **73**, (1998), p. 1991.

[2] O. Schultz, S. W. Glunz, and G. P. Willeke, *Progress in Photovoltaics: Research and Applications*. **12**, (2004), p. 553.

[3] M. A. Green, K. Emery, Y. Hishikawa, W. Warta, and E. D. Dunlop, *Progress in Photovoltaics: Research and Applications*. **20**, (2012), p. 12.

[4] J. Parkes, R. D. Tomlinson, and M. J. Hampshire, *Journal of Crystal Growth*. **20**, (1973), p. 315.

[5] P. Jackson, D. Hariskos, E. Lotter, S. Paetel, R. Wuerz, R. Menner, W. Wischmann, and M. Powalla, *Progress in Photovoltaics: Research and Applications*. **19**, (2011), p. 894.

[6] I. Repins, M. A. Contreras, B. Egaas, C. DeHart, J. Scharf, C. L. Perkins, B. To, and R. Noufi, *Progress in Photovoltaics: Research and Applications*. **16**, (2008), p. 235.

[7] M. A. Contreras, T. Nakada, M. Hongo, A. O. Pudov, and J. R. Sites, *3rd World Conference on Phorovolraic Energv Conversion* (2003).

[8] K. Kushiya, M. Tachiyuki, Y. Nagoya, A. Fujimaki, B. Sang, D. Okumura, M. Satoh, and O. Yamase, *Solar Energy Materials & Solar Cells*. **67**, (2001), p. 11.

[9] K. Kushiya, T. Nii, I. Sugiyama, Y. Sato, Y. Inamori, and H. Takeshita, *Japanese Journal of Applied Physics*. **35**, (1996), p. 4383.

[10] T. Nakada, M. Mizutani, Y. Hagiwara, and A. Kunioka, *Solar Energy Materials & Solar Cells*. **67,** (2001) p. 255.

[11] D. Hariskos, M. Ruckh, U. Rühle, T. Walter, H. W. Schock, J. Hedström, and L. Stolt, *Solar Energy Materials & Solar Cells*. **41-42**, (1996), p. 345.

[12] N. Naghavi1, S. Spiering, M. Powalla, B. Cavana, and D. Lincot, *Progress in Photovoltaics: Research and Applications*.**11**, (2003), p. 437.

[13] A.E. Becquerel, “Comptes Rendus”, (1839).

[14] J. Hedstrom, H. Ohlsen, M. Bodegard, A. Klyner, L. Stolt, D. Hariskos, M. Ruckh, and H.W. Schock, *23rd IEEE Photovoltaic Special Conference*, (1993) p. 364.

[15] D. W. Niles, K. Ramanathan1, F. Hasoon, R. Noufi, B. J. Tielsch, and J. E. Fulghum, *Journal of Vacuum Science & Technology*. **15**, (1997) p. 3044.

[16] K. Orgassa, H. W. Schock, and J. H. Werner, *Thin Solid Films*. **431-432,** (2003), p. 387.

[17] S. Mahieu, W. P. Leroy, K. V. Aeken, M. Wolter, J. Colaux, S. Lucas, G. Abadias, P. Matthys, and D. Depla, *Solar Energy Materials & Solar Cells*. **85** (2011) p. 538.

[18] D. Abou-Ras, G. Kostorz, D. Brémaud, M. Kaelin, F.V. Kurdesau, A.N. Tiwari, and M. Döbeli, *Thin Solid Films.* **480–481**, (2005), p. 433.

[19] T. Wada, N. Kohara, S. Nishiwaki, and T. Negami, *Thin Solid Films.* **387**, (2001), p. 118.

[20] S. Nishiwaki, N. Kohara, T. Negami, and T. Wada, *Japanese Journal of Applied Physics*. **37**, (1998), p. 71.

[21] A. M. Gabor, J. R. Tuttle, D. S. Albin, M. A. Contreras, R. Noufi, and A. M. Hermann, *Applied Physics Letters.* **65**, (1994), p. 198.

[22] R. Herberholz, U. Rau, H. W. Schock, T. Haalboom, T. Godecke, F. Ernst, C. Beilharz, K. W. Benz, and D. Cahen, *The European Physical Journal Applied Physics.* **6**, (1999), p. 131.

[23] D. Schmid, M. Ruckh, F. Grunwald, and H. W. Schock, *Journal of Applied Physics.* **73**, (1993), p. 2902.

[24] J. J. M. Binsma and H. A. van der Linden, *Thin Solid Films.* **97**, (1982), p. 237.

[25] T. L. Chu, S. S. Chu, S. C. Lin, and J. Yue, *Journal of the Electrochemical Society*. **131**, (1984), p. 2182.

[26] V. K. Kapur, B. M. Basol, and E.S. Tseng, *Solar Cells.* **21**, (1987), p. 65.

[27] J. F. Guillemoles, U. Rau, L. Kronik, H. W. Schock, and D. Cahen, *Advanced Materials.* **11**, (1999), p. 957.

[28] Z. Zhou, K. Zhao, and A. Rockett, *Japanese Journal of Applied Physics*. **49**, (2010), p.81202.

[29] J. A. Dean, "LANGE'S HANDBOOK OF CHEMISTRY", (1999).

[30] A. Goudarzi, G. M. Aval, R. Sahraei, H. Ahmadpoor, *Thin Solid Films.* **516**, (2008), p. 4953.

[31] T. Nakada, M. Hongo, and E. Hayashi, *Thin Solid Films.* **431-432**, (2003), p. 242.

[32] S. H. Wei, S. B. Zhang, and A. Zunger, *Applied Physics Letters.* **72**, (1998), p. 3199.

[33] T. Negami, T. Satoh, Y. Hashimoto, S. Shimakawa, S. Hayashi, M. Muro, H. Inoue, and M. Kitagawa , *Thin Solid Films*. **403-404**, (2002), p.197.

[34] E. P. Zaretskaya, V. F. Gremenok, V. B. Zalesski, K. Bente, S. Schorr, and S. Zukotynski, *Thin Solid Films.* **515**, (2007), p. 5848.

[35] A. Ennaoui, W. Eisele, M. Lux-Steiner, T. P. Niesen, and F. Karg, *Thin Solid Films.* **431-432**, (2003), p. 335.

[36] M. K. Ghosh, S. Anand, R. P. Das, *Hydrometallurgy.* **22**, (1989), p. 207.